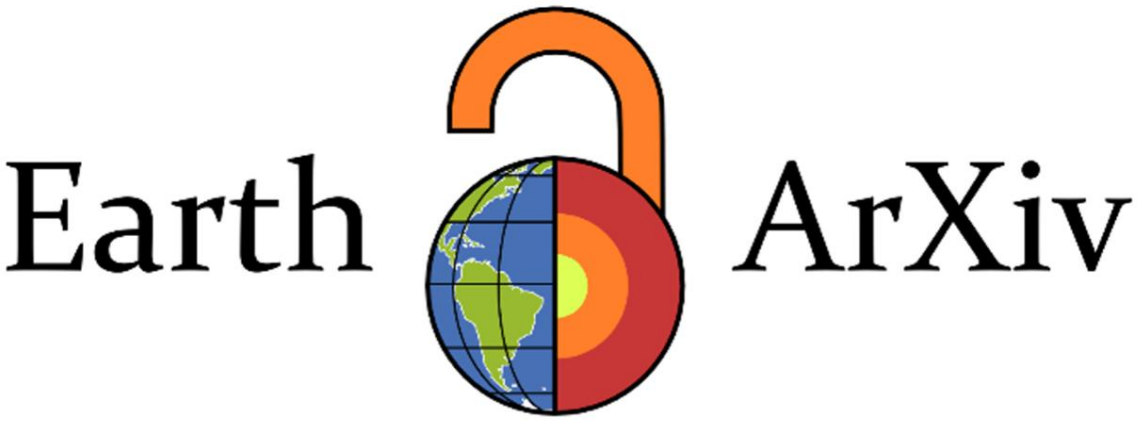

Peer review status:

This is a non-peer-reviewed preprint submission to EarthArXiv

This manuscript has been submitted for publication in Science of the Total Environment (STOTEN).

Smoothing Earth's surface: the complexity of soil texture class transitions

Trevan Flynn[*1], *Zahra Rasaei*[2], *Rosana Kostecki*[3,4]

[*1]Department of Agronomy, University of Forte Hare, Alice 5700 South Africa

[2]Department of Soil Science, University of Tehran, Karaj 77871 Iran

[3]Soil Consultoria Socioambiental, R. Prof. Joaquim de Matos Barreto, 88-Lima Azevedo, Londrina 86015 Brasil

[4]Department of Geography, State University of Londrina, Londrina 86055 Brasil

[*]Corresponding author email: trevanflynn@gmail.com

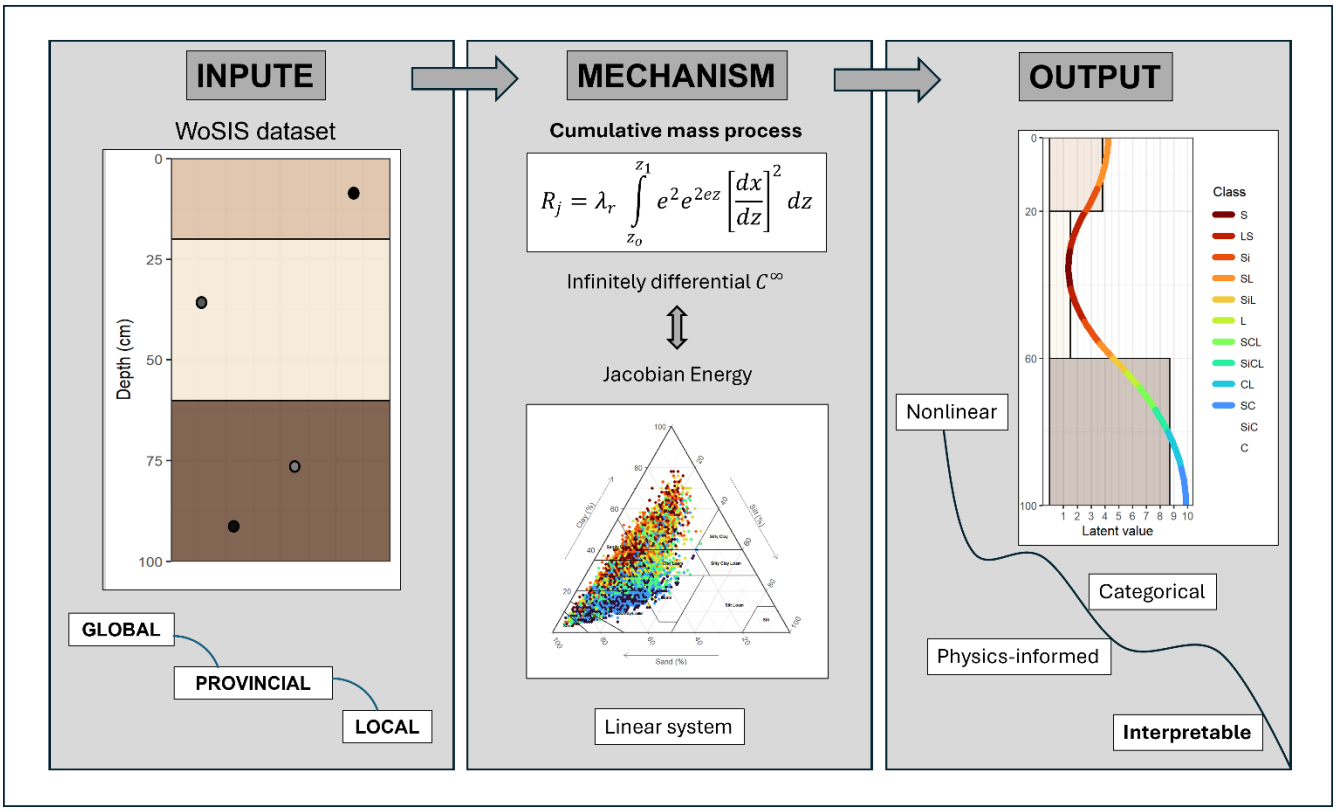

Abstract

Soil depth functions are essential for analysing, modeling, understanding and visualising soil profiles. While robust methods existed for continuous properties, soil texture is typically reported as discrete classes, and no established approach exists to interpolate soil categorical information with depth. Here, we introduced phySplines, a physics-informed, analytically solvable spline for interpolating soil categorical information. Soil texture classes were mapped to a latent numerical space and continuously interpolated by minimising the depth-weighted Jacobian energy via the exact analytic integral of Euler's cumulative mass process, which encoded depth-dependent resistance and enforces non-parametric physically consistent smoothness. PhySplines achieved kappa values of 0.96, 0.94 and 0.96 at global, provincial and local scales, respectively. By embedding pedological theory within a fully continuous and interpolation framework, the function avoided over representation of dominant classes, captured previously unmodelled transitional states, mitigated the drift effect and generalised across missing layers. PhySplines maintained mass and energy continuity (infinitely differentiable C^{∞}) without over-constraining the solution, allowing for greater flexibility for future work into numerical classification and the quantification of soil thermodynamical multifunctionality. Ultimately, minimising potential energy and maintaining the mass continuity, phySplines transformed complex soil profiles into dynamic, interpretable narratives, allowing users to "see" between horizons.

Keywords: Exact analytic integral; Depth function; Jacobian energy; Physics-informed

1 Introduction

Interpolation of properties with depth is a common practice across many scientific disciplines (Ma et al., 2026; Odom and Doctor, 2023; Probst et al., 2018; Rogozovsky et al., 2025; Zhao et al., 2025) and has become standard in soil analysis (Amundson et al., 2025; Benbi and Toor, 2026; Pei et al., 2025; Souza et al., 2023). Depth functions expand datasets by enabling harmonisation with other datasets (Cheng et al., 2024), improve understanding of soil profile physical (Zhang et al., 2023) and biochemical dynamics (Leewis et al., 2022) and support downstream applications in hydrology, ecology and environmental management (Ruiz et al., 2025). By providing representations that are mathematically robust yet easy to conceptualise and visualise, depth functions help facilitate communication with scientists, policymakers and communities.

Several approaches exist for representing soil properties with depth, including exponential decay (Kempen et al., 2011; Wiese et al., 2016), polynomials (Colwell, 1970; Russell and Moore, 1968), cubic splines (Flynn et al., 2022b), equal-area splines (ea-splines) (Bishop et al., 1999; Malone et al., 2009; Ponce-Hernandez et al., 1986) and grid-based ea-splines (Flynn et al., 2024). Unlike standard smoothing splines, ea-splines are formulated such that the integral of the spline equals the observed horizon mean, ensuring mass preservation with each horizon (Bishop et al., 1999; Ponce-Hernandez et al., 1986). Despite the benefits of continuous depth functions, limited soil profile observations may over-constrain them, leading to unrealistic values and increased criticism (Kienast-Brown et al., 2021).

Nevertheless, soil depth functions have rarely accommodated categorical data such as soil texture classes, which carry critical information for farmers, educators and land managers. The historical absence of robust methods for interpolating categorical data arises from the misconception that discrete soil classes do not exhibit boundary or transitional behavior (Burrough et al., 1997; Henderson et al., 2025) and partly from the inherent complexity of categorical mathematics (Basu and Isik, 2020; Yanofsky, 2015). Furthermore, traditional taxonomic dissemination tools are rarely designed for numerical modeling

(Zhang and Goodchild, 2002), creating bottlenecks that lead to information loss, computational inefficiency and a disconnect between soil taxonomy and the quantitative requirements of environmental models (Bortolus, 2008; Hillebrand et al., 2018; Isaac, 2004; Weiskopf et al., 2022).

The aim of this study was to develop phySplines, a physics-informed, analytically solvable spline for interpolating categorical soil information to standardised depths across global, provincial and local scales. Specifically, we sought to: (i) develop fully continuous, differentiable and mass-preserving categorical splines that maintain pedological realism across spatial supports; (ii) incorporate physics-informed constraints into an analytically solvable formulation, providing insight into class behaviour while remaining computationally scalable without over-constraining; and (iii) develop a deterministic spline capable of predicting "unseen" categories and inferring transitional or boundary classes suggested by depth gradients, even when such classes were not directly observed in the profile. These innovations introduce pedological realism by enforcing continuous, process-based gradients and transitions, effectively bridging taxonomic information with the rigorous requirements of numerical environmental modeling.

2 Methods and materials

2.1 Soil observations

To evaluate whether phySplines can be applied globally, across different spatial supports and for various purposes, the spline was tested at three spatial scales. Data was obtained from the World Soil Information Systems (WoSIS) dataset (ISRIC, 2021), which provides nearly global coverage. The global scale encompassed most of the soil forming factors as well as soil functions that contribute to society and the environment. Observations were included for analysis if they had United States Department of Agriculture (USDA) soil texture classes assigned or had clay, silt and sand fractions summing to 100% and the soil depth was $\leq$200 cm. A depth limit of 200 cm was applied because most international and

national soil classification systems, including the World Reference Base (WRB) and USDA Soil Taxonomy, do not define diagnostic criteria beyond this depth. After filtering, a total of 101,568 soil observations were retained for global analysis with or without missing horizons.

The WoSIS dataset included 6,791 observations (0.008 samples km^{-2}) at the provincial scale across New South Wales (NSW), Australia (Figure 1), covering approximately 801,150 km^2 (center ≈147°1′E to 32°9′S). Elevation ranges from sea level to >2,000 m in the southeastern highlands. The geology is unique with distinct sedimentary basins, with widespread sodic soil formed during episodes of landscape uplift (Blewett, 2012). Climate and vegetation are highly variable across the province (Australian Bureau Of Meteorology, 2019) with both winter and summer cropping systems represented (McDougall et al., 2002; NSW Department of Primary Industries, 2020). Major urban centres are concentrated along the coast, whereas inland areas are predominantly rural and agriculturally oriented (Smith and Robert B. Thompson, 2019). The province was selected because it is among the most extensively studied regions in quantitative pedology (e.g., the Hunter Valley), nearly all available profiles met the study criteria (<200 cm depth and particle-size fractions summing to 100%) and the province encompasses a broad range of environmental conditions relevant to pedogenesis.

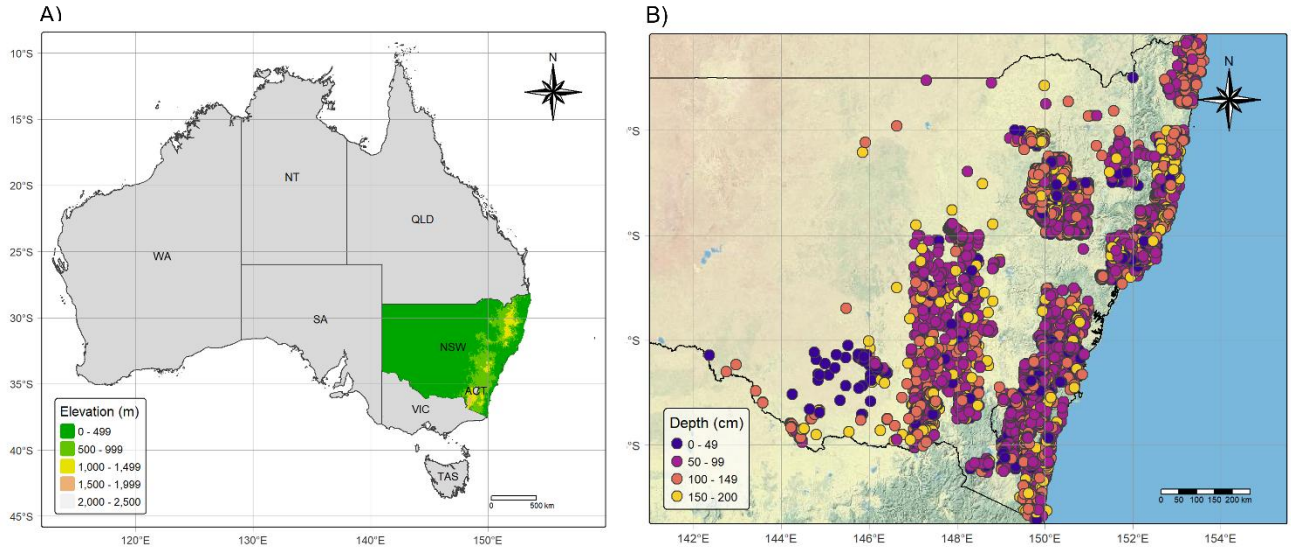

Figure 1: The elevation of New South Wales (NSW) within Australia (A) and the soil observations with depth of NSW (B).

A region in southern Malawi (center ≈34°41′42″E, 15°26′42″S) was selected to evaluate phySplines at the local scale due to the relatively high number of WoSIS soil observations (0.05 samples km^{-2}) within a 1,191 km² area (Figure 2). Located northwest of Blantyre in the Neno District, there were 65 profiles within and around a valley to the Lisungwe River, which drains to the Shire River, the primary outlet of Lake Malawi. The elevation ranges from 256 to 1,635 m, corresponding to strong gradients in mean annual temperature and precipitation (Fick and Hijmans, 2017). The region has a subtropical Udic soil moisture regime and is dominated by smallholder agriculture, including tobacco, cotton, maize, soybean and groundnut production (Araya et al., 2023). This site was selected because it provides sufficient profile density to evaluate local-scale model behaviour and represents an environmentally sensitive landscape relevant to soil–water and land-use management.

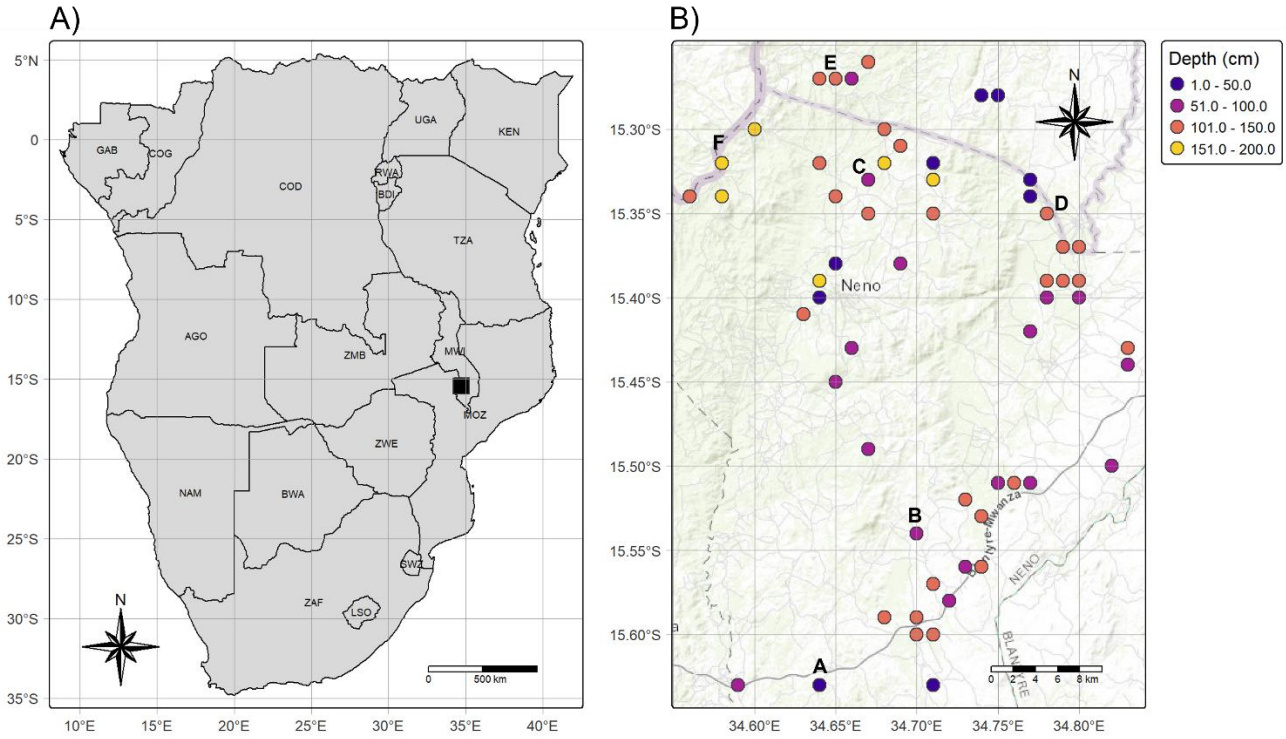

Figure 2: Neno District (not to scale), Malawi within southern Africa (A) and the soil samples with depth within Neno District (B).

Cross-scale validation was used to explicitly test the sensitivity of phySpline to observation density and spatial heterogeneity. The global dataset spans highly variable soil environments with uneven sampling

densities, the NSW dataset represents a spatially biased setting with moderate observational support, and the Neno dataset reflects a dense but spatially constrained context. Consistent performance across these scales indicates that phySpline does not depend on scale-specific tuning or regional calibration, but instead derives stability from its physically constrained formulation.

For all scales, USDA soil texture classes comprised 12 categories, derived from clay, silt, and sand fractions on a texture triangle. The natural ordinal rank, from sand (1) to clay (1), was used for the physical process representing particle mass and surface area from the smallest to largest; the data was treated as unranked ordinal. Table 1 summarises the class symbols, names, latent value and the number of observations at the global, provincial and local scales.

Table 1: The United States Department of Agriculture (USDA) soil texture class symbol, name, latent value (Order) and the number of observations (n) for the global, provincial and local scales.

Class	Name	Order	Global (n)	Provincial (n)	Local (n)
S	Sand	1	28,390	824	3
LS	Loamy sand	2	28,511	1,400	50
Si	Silt	3	1,983	3	0
SL	Sandy loam	4	77,663	3,869	60
SiL	Silty loam	5	70,733	83	0
L	Loam	6	60,196	943	1
SCL	Sandy clay loam	7	35,856	4,024	56
SiCL	Silty clay loam	8	40,116	47	0
CL	Clay loam	9	35,977	1102	0
SC	Sandy clay	10	10,394	1,184	30
SiC	Silty clay	11	22,543	57	0
C	Clay	12	67,364	9,044	12

2.2 PhySpline theory

PhySplines are an energy-minimising function fitted through an exact integral function derived from classical mechanics. Along with the conservation of mass, the spline is based on potential energy, where the curve adjusts to maintain minimal energy through the cumulative mass of the soil column and boundary conditions with the surface, lithosphere and hydrosphere. In this case, we imposed a mathematical steady state by enforcing a zero flux and a geogenic steady state for the top and bottom horizons, respectively. Therefore, along with mass conservation, we enforce mass and energy continuity in a fully continuous, non-parametric function and move away from geometric midpoints toward the exact integral of the minimised energy.

2.2.1 Fundamental concept

To enable the use of categorical soil data, discrete soil texture classes were first mapped onto an ordered latent numerical axis by class symbols with order (Table 1). This ordinal transformation preserves the natural progression of texture from coarse to fine, allowing interpolation in continuous space while retaining categorical interpretability. Although soil texture triangles are conventionally defined by sand, silt and clay, the latent mapping flattened this multi-dimensional space into a one-dimensional sequence, with sand and clay as the endmembers. This simplification converts the complex multi-dimensional problem into a standard depth function, facilitating spline interpolation and process-based interpretation. This approach assumes that soil texture classes can be treated as ordinal data.

Each spline segment self-regularises, stiffening naturally with cumulative horizon mass according to an exponential process Euler's (e) cumulative mass process, effectively following a steady-state definite integral that limits unrealistic slopes. Latent values were then mapped to the nearest soil texture classes to produce harmonised, physically consistent profiles. Profile harmonisation was achieved by integrating the fitted latent values to the GlobalSoilMap standard depth intervals (0–5, 5–15, 15–30, 30–60, 60–100

and 100–200 cm). The harmonised dataset, source code, and the rafikisol R package (Flynn, 2023) are available at www.github.com/rafikisol/rafikisol.

Key components of the phySpline formulation include:

- Continuous data fidelity: Observations contribute through a fully continuous loss function, integrating across horizon thicknesses rather than relying on geometric midpoints.
- Definite integral: The spline was coefficients were estimated using the exact integral for the entire profile, being infinite differentiable C^{∞}.
- Boundary conditions: The constraint matrix anchored the slope at the top and bottom, ensuring the profile naturally returned to vertical at the boundaries.
- Physics-informed regularisation: The splines curve is dependent on the cumulative mass above in a continuous manner from the Euler's cumulative mass process.
- Explicit matrix formulation: The design matrix A, regularisation matrix R and Jacobian constraint matrix G are fully specified, enabling direct and transparent control over constraint enforcement.
- Inter-horizon continuity: Continuity of both values (C^0) and first derivatives (C^1) are enforced across horizon boundaries via a null-space projection of G, ensuring physically informed constraints are satisfied exactly.
- Latent class preservation: Continuous latent values are mapped back to discrete soil texture classes, maintaining interpretability while enabling continuous interpolation.

These central concepts of the phySpline go along with the paradigm shift in depth functions as we move away functions that produce unrealist estimates. However, instead of using the point depth approach like the USDA digital soil mapping focus team (Kienast-Brown et al., 2021); we decided to make sure the spline was pedologically realistic, not over-constrained and obeyed physical laws.

2.2.2 Potential energy of soil

In phySplines, the soil profile is represented as a one-dimensional scalar field evolving within a potential-energy framework, where profile smoothness corresponds to the energetic cost of deformation. Since potential energy is defined through spatial gradients, this formulation aligns with pedological theory, in which soil profiles result from gravity-driven transport, diffusion and kinetically limited processes acting over depth and time (Hillel, 1998). This framework is not limited to pedology but is applicable across scientific disciplines, where potential energy provide the thermodynamic basis of soil multifunctionality and the capacity of soils to deliver ecosystem services (Kleidon, 2010). Therefore, this is not a random physics-informed theory, but one that is pedologically relevant and connects across disciplines, enhancing communication.

Within this framework, the soil profile is modeled as a scalar field $f(z)$embedded in a heterogeneous medium with a depth-dependent resistance function $D(z)$. Under steady-state conditions, the profile minimises a weighted Dirichlet energy and satisfies the Euler–Lagrange equation:

$$\frac{d}{dz}\left(D(z)\frac{df(dz)}{dz}\right) = 0$$

with corresponding potential energy functional:

$$E[f] = \frac{1}{2}\int_{o}^{H} D(z)\left(\frac{df}{dz}\right)^{2} dz$$

Here, $D(z)$ represents the local energetic resistance to slope change, reflecting mechanical and structural constraints of deeper soil layers due to compaction, overburden, clay illuviation and reduced biological mixing. This formulation naturally permits greater flexibility near the surface while progressively constraining curvature at depth, producing smooth and physically consistent profiles.

To model the monotonic increase in resistance while retaining analytical tractability, $D(z)$ is expressed as an exponential function:

$$D(z) = D_o e^{kz}$$

which arises from the assumption that resistance increases proportionally to its current magnitude. The exponential form of the resistance function arises naturally as the solution to a first-order growth process, where the rate of change in soil stiffness is proportional to its current magnitude. The parameter k represents the attenuation coefficient of pedological influence, while z defines the latent taxonomic intensity, providing a coordinate system where physical stability is linked directly to the soil's developmental state. The inclusion of Euler's number e ensures that this increase in resistance with depth is both continuous and scale-independent.

2.2.3 Physics-informed spline

The phySpline theory is expressed directly through the equations used in implementation, ensuring that the mathematical formulation and computational realization are identical. The phySpline for each horizon was expressed as a piecewise quadratic function:

$$f_j(x) = \alpha_j + b_j(x - u_j) + \gamma_j(x - u_j)^2,$$

where $\alpha_j$is the value at the top of horizon j, b_j is the slope at the top of the horizon, γ_j controls the curvature of the function within the horizon, and u_j is the top depth of horizon j. The curvature term γ_j governs the redistribution of slope with depth, allowing internal deformation while maintaining continuity at horizon boundaries. To estimate the coefficients $\beta = (\alpha_j, b_j, \gamma_j)$, data fidelity, regularisation (roughness control), and inter-horizon continuity must be jointly enforced.

The data fidelity loss function was formulated as the continuous integral over each horizon to preserve the exact mean, numerical stability and class structure.

$$L(A) = \frac{1}{2}||y - \mathrm{A}\beta||_2^2 = \frac{1}{n}\sum_{j=1}^{n}\left(\int_0^{h_j} f_j(x)dx - y_j\right)^2$$

where h_j is the thickness of horizon j and the integral measures the squared difference between the spline-interpolated values $f_j(x)$ and the observed values y_j.

For the regularization term, pedological theory governs the conceptual model, physics governs the horizons, with smoothness arising from the minimisation of potential energy within each horizon. Spline smoothness was governed by a depth-weighted Jacobian energy defined through the exact analytic integral of a global Euler cumulative mass process. Rather than treating regularisation as a numerical penalty or imposing boundary conditions, the energetic cost of deformation was integrated over each horizon, allowing smoothness and curvature to emerge naturally from the profile itself. For horizon j, the energy minimised was

$$R_j = \lambda_r \int_{z_o}^{z_1} e^2 e^{2ez}\left[\frac{dx}{dz}\right]^2 dz$$

Where the exact analytic integral is infinitely continuous across the z_0 and z_1 normalised thickness $z \in [0, 1]$. The exponential term represents a depth-dependent stiffness, reflecting increasing mechanical and structural resistance with depth, while the difference-quotient formulation evaluated resistance as a physically meaningful process that is infinitely differentiable C^∞. Cumulative mass resistance was defined globally and integrated over finite horizons creating boundary behaviour that emerged naturally from the exact analytic integral. Therefore, the top horizon collapses to a point evaluation at $z = 0$, the basal horizon to $z = 1$ and interior horizons are governed by the integral means of the stiffness process. Smoothing was thus confined strictly to the soil domain, preventing boundary drift, align with the constraint matrix, while maintaining physically consistent continuity and curvature.

Data continuity between horizons represents a physical requirement for mass conservation and structural integrity. These constraints were encoded in a Jacobian matrix G, enforcing both C^0 and C^1 continuity across horizons:

$$\|G\beta\|_2^2 = G\beta = 0,$$

$$f_j(h_j) - f_{j+1}(0) = 0 \ \ (\mathrm{C}^0\ continuity),$$

$$f_j'(h_j) - f_{j+1}'(0) = 0 \ \ (\mathrm{C}^1\ \mathrm{continuity}),$$

Boundary slope constraints were applied at the top and bottom of the profile to anchor the spline, maintain numerical stability and maintain a mathematically steady state. Together with R, the boundary conditions create a zero flux and geogenic boundary for the top and bottom horizon, respectively. To enforce all constraints exactly while retaining a linear system, the coefficient vector was projected into the null-space of G:

$$\beta = N\gamma,$$

where N spans the null-space of G. Within this projected space, the horizon-level roughness penalties $R_j$are combined into a global, profile-aware roughness matrix, representing the total energetic cost of profile deformation:

$$R = N^T\left(\sum_j R_j\right)N$$

This transformation converts the constrained energy minimisation problem into an unconstrained system in γ, ensuring exact horizon continuity while preserving the physical interpretability of the roughness penalty. In this way, continuity constraints were satisfied exactly, the roughness penalty remained

physically interpretable and the solution efficiently balances fidelity to observed data with minimisation of the profile's potential energy. The objective function is then formulated as:

$$\mathcal{L}(\gamma) = \frac{1}{2} \| y - AN\gamma \|_2^2 + \lambda_r \gamma^\top N^\top R N \gamma.$$

Solving for γ yields the reduced-order ordinary least squares solution, and the full coefficient vector is recovered as $\beta = N\gamma$. This approach guarantees exact horizon continuity while balancing smoothness against fidelity to the observed data. Crucially, the roughness term R arises from the definite integral of the Euler cumulative mass process, embedding global, depth-dependent stiffness directly into the loss function. The governing system is linear and reflects steady-state physics, and the phySpline solution is obtained analytically through energy minimisation, producing an optimal, closed-form set of coefficients that captures physically consistent curvature and emergent boundary behaviour across the profile.

Once a spline's coefficients were estimated, the integral for any standardised depth interval can be directly calculated or continuous curves can be interpolated and fitted values $f_i(x)$ are mapped to soil classes by nearest latent class (Table 1):

$$c_i = \arg\min_i | f_i(x) - l_i |,$$

where l_i are latent class values and c_i is the interpolated soil texture class at location (e.g., interval, cm, mm, etc) i. This approach provides a simple, computationally efficient and intuitive classification of the full vertical soil profile.

2.2.4 Generalisation and missing horizons

Many studies have discussed the idea of adding pseudo horizons to anchor boundary conditions at the top and bottom of the profile or as an anchor when there are discrete boundaries (Bishop et al., 1999; Malone et al., 2009; Odgers et al., 2012; Ponce-Hernandez et al., 1986). Notably, many authors noted challenges with abrupt changes or the "drift" effect common in quadratic splines. To handle missing or

unsampled depths, pseudo horizons were introduced to stabilise phySpline coefficients. Missing depths were initially imputed using the median of adjacent horizons, providing placeholders for coefficient estimation. Once spline coefficients were computed, imputed horizons were removed from the system and treated as extrapolated regions. However, no pseudo-horizon was added to address drift, as the energy-minimising solution naturally curves back to a vertical slope.

2.2.5 Spatial prediction

At the provincial scale, harmonised soil texture classes were predicted across the 90 m Soil and Landscape Grids of Australia (ASRIS, 2024; CSIRO, 2024) to provide spatial representations and visualise vertical variation along transects. Predictions were generated for six standard depth intervals, using 18 covariates representing clay, silt, and sand fractions within each depth interval (Malone and Searle, 2022; Viscarra Rossel et al., 2014). Gradient tree boosting was used for spatial prediction due to its ability to capture complex environmental relationships without over-predicting dominant soil classes (Flynn et al., 2019). Gradient tree boosting is an eager learner that precomputes a model during training (from soil profiles), making prediction across grids computationally efficient (Hastie et al., 2009; Kuhn and Johnson, 2013). For each depth interval, all grid layers were used as covariates, i.e., the independent variables consisted of texture fractions from 0–200 cm. Mathematically, the predicted soil texture class $\hat{C}_k$ for class k is:

$$\hat{C}_k \approx \sum_{m=1}^{M} L_m H_m(clay_k, silt_k, sand_k),$$

where M is the total number of trees, L_m is the learning rate, and H_m is the m-th tree in the sequence, trained to iteratively improve predictions from the previous tree.

2.3 Validation and plausibility

2.3.1 Reference splines

Two reference splines (controls) were implemented to illustrate the methodological progression from standard continuous interpolation to the phySpline framework. This progression is intended as a demonstration of specific enhancements, rather than a formal comparative study, highlighting the steps required to resolve categorical transitions while retaining the simplicity and statistical robustness of the ea-spline framework.

The first reference spline, C-EAS was a canonical ea-spline adapted to classify where data fidelity was the geometric mean, and the regularization term was the first derivative penalty. Therefore, continuity is implicitly implied through the geometry of the fidelity term

$$\mathcal{L}_{C-EAS}(\beta) = \frac{1}{2}||A\beta - y||_2^2 + \lambda_r \beta R \beta.$$

The C-SoftG reference spline was a non-canonical intermediate spline where there is a trade off between data fidelity, smoothness and continuity. The terms are the same as the ea-spline and continuity matrix is the same as the phySplines,

$$\mathcal{L}_{C-SoftG}(\beta) = \frac{1}{2}||A\beta - y||_2^2 + \lambda_r \beta R \beta + ||G\beta||_2^2.$$

2.3.2 Statistical validation

PhySpline performance was evaluated across multiple scales using overall accuracy, Cohen's kappa (Cohen, 1960) and the latent value Root Mean Squared Error (RMSE) for λ_r values of 0.5, 0.25, 0.10, 0.05 and 0.01. These values were selected following Bishop et al. (1999) and other studies on ea-splines such as Malone et al. (2009) and . This approach ensured that scale-specific performance reflected robustness to data availability, rather than simply spatial extent, providing a controlled stress test. To

select an appropriate λ_r for the control and subsequent analyses, a sensitivity analysis was performed using L-curve curvature maximisation at the global scale. The "elbow" of the curve, corresponding to the peak of the second derivative of the LOESS-smoothed RMSE profile, identifies the transition between under- and over-fitting.

For individual soil texture classes, recall (producer's accuracy), precision (user's accuracy), bias and F1 scores were calculated to evaluate the ability of phySplines to classify both dominant and underrepresented classes. Harmonised uncertainties were quantified as the absolute distance between predicted values and the nearest latent class, providing a measure of confidence across both occupancy and transitional classes. These uncertainties were subsequently scaled to a range of 0–1.

Spatial predictions were evaluated in a similar manner, using an 80/20 split for training and evaluation. Overall accuracy was computed to assess predictive performance. While the primary focus of this study is phySpline performance, evaluation of spatial predictions ensured that mapped representations of soil texture are meaningful, reliable for visualisation purposes and were comparable to other studies.

2.3.3 Physical plausibility

To evaluate the behaviour and physical consistency of the phySpline solutions, we computed a set of diagnostics for profile:

- Kink (C^1 Continuity): The absolute difference between the bottom slope of one horizon and the top slope of the next, capturing derivative discontinuities at horizon boundaries.
- Energy (Roughness): The quadratic form $\beta^T R_s \beta$ for each horizon, representing the contribution of the horizon to the spline's regularisation term. Higher energy indicates significant internal "stretching" to accommodate the data.

- Mass jump (Mass): The ratio of horizon thickness h_j to the total profile depth H_{tot}, representing the volumetric leverage of the layer.
- Mismatch (C^0 Continuity): The absolute difference between the predicted value at the base of horizon $j$and the intercept of horizon $j+1$, quantifying value discontinuities across horizons.

These diagnostics provide complementary measures of smoothness, physical realism, and horizon-level behavior, allowing both global and horizon-specific assessment of spline performance.

To summarise spline physical plausibility, we combined the diagnostics into a composite metric. Let K_i denote the interfacial kink, E_i the internal energy, M_j the horizon mass jump, and $M_{m,i}$ the boundary mismatch. Weighted root-mean-square (RMS) values were computed for kink and energy as:

$$\mathrm{K_{RMS}} = \sqrt{\frac{\sum_{i=1}^{n}(K_i\, M_j)^2}{\sum_{i=1}^{n} M_j}}$$

$$\mathrm{E_{RMS}} = \sqrt{\frac{\sum_{i=1}^{n}(E_i\, M_j)^2}{\sum_{i=1}^{n} M_j}}.$$

The RMS of mismatch is calculated as:

$$\mathrm{Mismatch_{RMS}} = \sqrt{\frac{1}{n}\sum_{i=1}^{n} M_{m,i}^2}\,.$$

Weighting kink and energy by M_j ensures that structural integrity of the primary soil mass is prioritized over localized noise in thin horizons. The Integrated Process Score (ISP) metric is then defined as the average of these three RMS values:

$$\mathrm{ISP} = \frac{\mathrm{Kink}_{\mathrm{RMS}} + \mathrm{Energy}_{\mathrm{RMS}} + \mathrm{Mismatch}_{\mathrm{RMS}}}{3}.$$

To assess whether predicted classes preserve information from observed classes, Mutual Information (MI) was calculated:

$$I(X;Y) = \sum_{x\in X}\sum_{y\in Y} p(x,y)\log\left(\frac{p(x,y)}{p(x)p(y)}\right),$$

where X is the observed soil texture class, Y the predicted class, $p(x,y)$ the joint probability of $X = x$ and $Y = y$, and $p(x)$, $p(y)$ the marginal probabilities. MI was normalized to the range [0,1] by dividing by the maximum MI within each group. This captures transitions across the two-dimensional structure of Depth × Classes [1–12], which would be missed in a one-dimensional, depth-only analysis (e.g., continuous depth).

This formulation favors economical, process-clamped solutions, where latent profiles transition smoothly with depth. It serves as a structural validation metric, ensuring that spline-derived numeric values produce a physically consistent soil column before categorical assignment. In other words, MI quantifies how much information the predictions preserve about observed classes while maintaining realistic, depth-continuous transitions.

3 Results

3.1 Comparisons

The results of the phySpline at each scale followed the same general pattern (Table 2). As λ_r decreased, phySpline performance increased, with higher accuracy, kappa values and lower latent-space errors.

These patterns, however, were most pronounced at the global scale with an 80% reduction in λ_r (from 0.50 to 0.10) resulting in a 44% increase in kappa, from 0.76 to 0.95. A further 90% reduction in λ_r (from 0.10 to 0.01) was associated with a 4% increase in kappa, from 0.95 to 0.99. The corresponding RMSE decreased from 0.37 at $\lambda_r = 0.50$ to 0.13 at $\lambda_r = 0.10$ (65% decrease in errors), and further to 0.02 at λ_r= 0.01 (85% decrease in errors). Therefore, there is a strong relationship between λ_r, accuracy, kappa and RMSE. Thus, the elbow method on the global data revealed a λ_r = 0.10 was the slope steepened past this point indicating potential overfitting.

Table 2: The scale, lambda (λ_r), overall accuracy, kappa and the latent RMSE.

Scale	λ_r	Accuracy (%)	Kappa	RMSE
Global	0.50	70	0.66	0.37
	0.25	89	0.89	0.21
	0.10	97	0.96	0.11
	0.05	100	1.00	0.01
	0.01	100	0.99	0.02
Provincial	0.50	77	0.72	0.37
	0.25	87	0.83	0.25
	0.10	96	0.94	0.13
	0.05	100	0.99	0.02
	0.01	100	1.00	0.02
Local	0.50	78	0.72	0.34
	0.25	92	0.89	0.23
	0.10	97	0.96	0.12
	0.05	100	1.00	0.01
	0.01	100	1.00	0.02

At the provincial scale, kappa increased from 0.66 at $\lambda_r = 0.50$ to 0.94 at $\lambda_r = 0.10$, reaching 1.00 at $\lambda_r = 0.05$. Over the same range, RMSE decreased from 0.37 to 0.13 and then to 0.02. over the same range. At the local scale, kappa increased from 0.72 at $\lambda_r = 0.50$ to 0.96 at $\lambda_r = 0.10$, and to 1.00 at $\lambda_r = 0.05$. The RMSE decreased from 0.34 to 0.12 and to 0.02 across the same range.

The C-SoftG control achieved statistical performance comparable to phySpline across all scales (Table 3). At the global scale, accuracy reached 97%, with a kappa of 0.96 and an RMSE of 0.14. At the provincial scale, accuracy, kappa, and RMSE were 95%, 0.90, and 0.14, respectively. At the local scale, C-SoftG achieved an accuracy of 93%, a kappa of 0.90, and an RMSE of 0.19. The C-EAS had nearly perfect statistical performance at all scales.

Table 3: The reference splinel accuracy-based measures showing the scale, λ_r, overall accuracy, kappa, RMSE of the residuals and the uncertainties of the harmonised depth intervals.

Spline	Scale	λ_r	Accuracy	Kappa	RMSE
C-SoftG	Global	0.10	97	0.96	0.14
	Provincial	0.10	95	0.93	0.14
	Local	0.10	93	0.90	0.19
C-EAS	Global	0.10	100	1.00	<0.01
	Provincial	0.10	100	1.00	<0.01
	Local	0.10	100	1.00	<0.01

At all scales, the IPS is comparatively lower with 0.15, 0.31 and 0.15 for the global, provincial and local scales respectively. However, all indices were best performing at the global scale with the lowest IPS and highest MI (1.00). The provincial scale, similar to the statistical analysis, had moderate performance with a slightly higher MI of 0.85 and the local scale had a MI of 0.88. It should be noted that these results are not comparable across models as the curves are fitted in different ways and the energy indicates a

different measure. However, the C-SoftG had the same trend and C-EAS techniqually doesn't have these measures but were gathered anyways to see if they were like the statistics and produce misleading results.

Table 4: Process based parameters showing mean energy, kink, MassJump, mismatch, Integrated Process Score (IPS) and Mutual Information (MI).

Spline	Scale	Kink	Energy	MassJump	Mismatch	IPS	MI
phySpline	Global	0.00	0.14	0.20	0.00	0.15	1.00
	Provincial	0.00	0.58	0.29	0.00	0.31	0.85
	Local	0.00	0.49	0.30	0.00	0.15	0.88
C-SoftG	Global	0.01	0.26	0.20	0.41	0.43	0.94
	Provincial	0.00	0.60	0.29	4.00	3.14	0.85
	Local	0.00	0.61	0.30	1.85	1.69	0.85
C-EAS	Global	0.00	0.00	0.20	17.7	9.60	1.00
	Provincial	0.00	0.00	0.29	23.0	11.5	1.00
	Local	0.00	0.00	0.30	16.6	7.60	1.00

.

Figure 3A–C presents example soil profiles illustrating continuity, mismatch, kink behavior and class–process alignment for the three models. The phySpline (Figure 3A) produced a smooth latent profile that crossed horizon boundaries exactly at observed class transitions while also resolving intermediate transitional classes along the latent scale. In contrast, the C-SoftG model correctly interpolated each horizon to its observed class but showed erratic curvature and limited representation of transitional classes between horizons (Figure 3B). The C-EAS model achieved perfect classification accuracy; however, the fitted curve and resulting classes strictly followed horizon boundaries allowing no transitory behaviour, yielding no meaningful internal structure beyond exact mathematical conformity (Figure 3C).

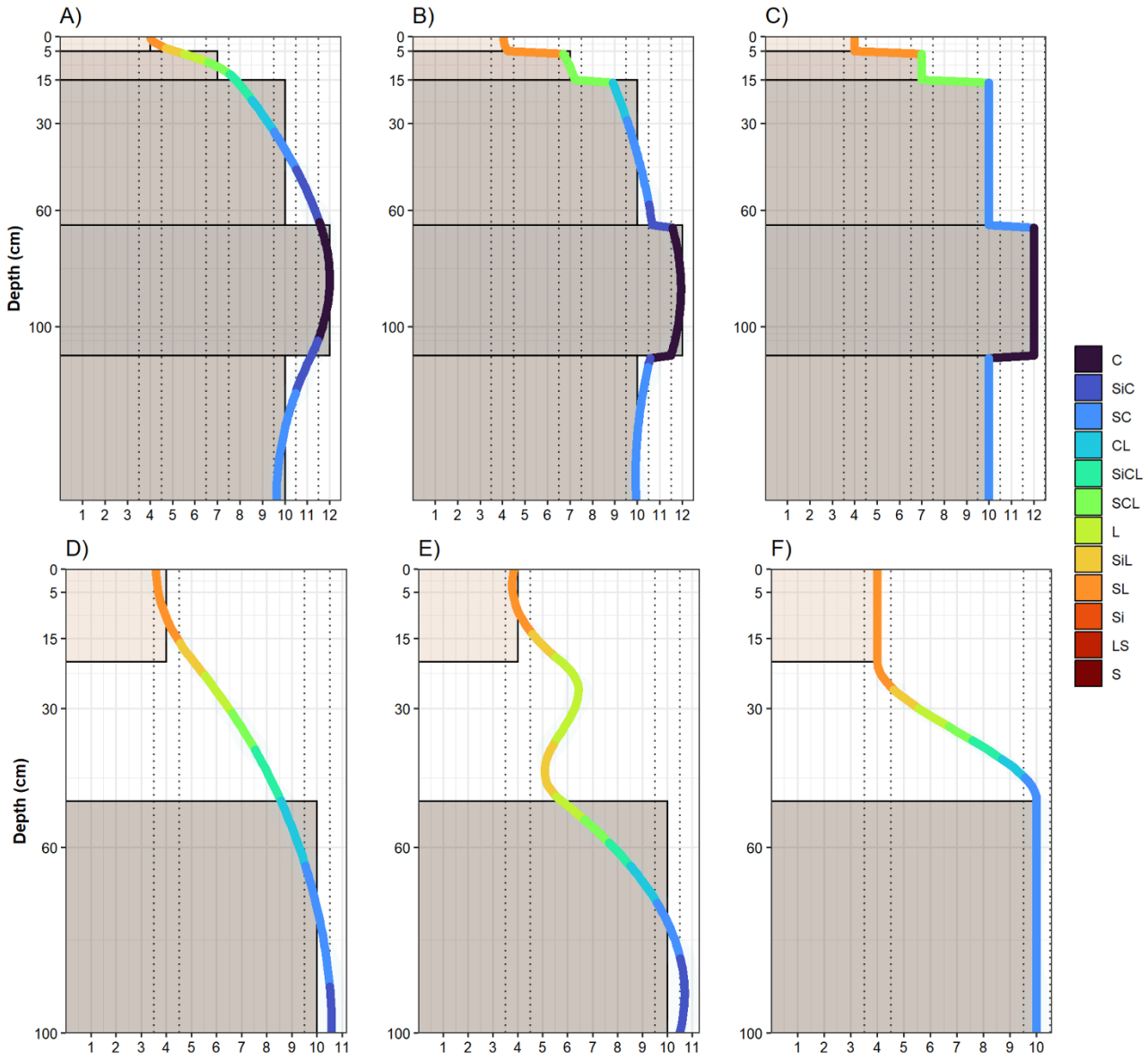

Figure 3: Selected profiles to demonstrate curves from the phySpline (A), the control C-SoftG (B), the control (C), missing horizons with phySplines (D), C-SoftG without ghost horizons (E) and C-EAS without ghost horizons (F).

Figure 3E–G show extrapolated profiles for the phySpline, C-SoftG (without a ghost horizon) and C-EAS (without a ghost horizon). The phySpline maintained smooth, physically coherent transitions under extrapolation (Figure 3E), whereas the absence of a ghost horizon in C-SoftG resulted in increased instability near profile boundaries (Figure 3F). The C-SoftG model was evaluated without a ghost horizon to illustrate the effects of extrapolation in the absence of artificial anchoring, whereas ghost horizons

were used for all other C-SoftG analyses. Notably, C-EAS captured transitional classes more effectively when horizons were absent, but this behavior was suppressed when horizons were present (Figure 3G).

3.2 Global scale

The global model took 8 min and 40.09 seconds to run 101,568 profiles through the linear ODE equation. Despite moderate class imbalance (observed occurrence ranging from 16.2% for SL to 0.41% for Si), all classes achieved F1 scores ≥ 0.80 except Si (F1 = 0.58; Table 4). Absolute occupancy bias remained within ± 1.00 percentage points for all classes except C (– 1.20), with the C class (14.0% observed occupancy) slightly underpredicted. The Si class exhibited high recall (0.90) but low precision (0.43), reflecting increased false-positive assignment for this rare texture class, which was slightly over predicted. All other soil texture classes had unbiased predictions according to a 1.00% threshold.

Table 5: The observed prevalence and predicted prevalence, prediction bias, precision, recall and F1 scores at the global scale.

Class	Observed (%)	Predicted (%)	Bias	Precision	Recall	F1
C	14.0	12.8	-1.20	1.00	0.91	0.95
SiC	4.70	5.28	0.58	0.78	0.87	0.82
SC	2.17	2.70	0.54	0.74	0.92	0.82
CL	7.50	7.25	-0.25	0.95	0.92	0.93
SiCL	8.36	8.56	0.19	0.92	0.94	0.93
SCL	7.47	7.71	0.24	0.91	0.93	0.92
L	12.6	13.1	0.58	0.91	0.95	0.93
SiL	14.7	14.6	-0.11	0.95	0.93	0.94
SL	16.2	15.5	-0.64	0.99	0.95	0.97
Si	0.41	0.86	0.45	0.43	0.90	0.58
LS	5.94	5.91	-0.04	0.95	0.94	0.94
S	5.91	5.59	-0.33	0.99	0.94	0.97

Class occupancy of harmonised depth intervals revealed systematic vertical trends in global soil texture distributions (Figure 4). Clay content increased with depth, rising from 9.40% at 5–15 cm to 16.60% at 60–100 cm (76% increase). However, stronger depth-related increases were observed for SiC and SC. The SiC class increased from 2.73% at 0–5 cm to 5.81% at 30–60 cm (113% increase), followed by a

slight decline to 5.09% at 100–200 cm. SC increased from 1.79% at 0–5 cm to 4.75% at 60–100 cm (166% increase). Both SiC and SC exhibited higher associated uncertainty, with mean uncertainty values of 0.27 and 0.39, respectively. Silty loam decreased from 19.8% at 5–15 cm to 10.9% at 60–100 cm (45% change), while SL declined from 18.7% at 0–5 cm to 11.5% at 100–200 cm (38% change). These classes exhibited comparatively low median uncertainty (0.15 for SiL and 0.14 for SL). In contrast, S showed minimal depth dependence, with only a 31% change across the profile, decreasing to 23% occupancy at depth.

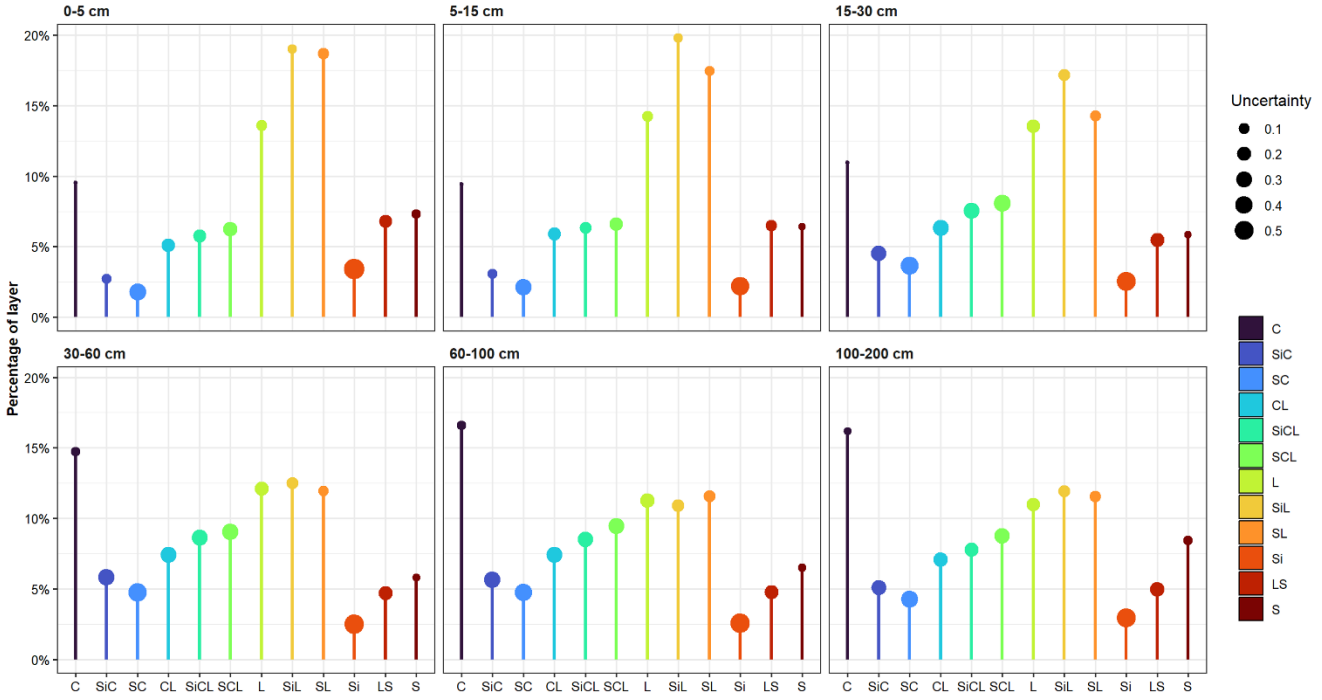

Figure 4: The percent proportion of each soil texture class for the GlobalSoilMap depth intervals with their uncertainties.

Depth-resolved structural diagnostics of the phySpline profiles revealed systematic variation across the harmonised depth intervals (Table 6). The phySpline was computationally zero for kink and mismatch was expected. For energy, it ranged from 0.314 at 100-200 cm to 0.493 at the 0-5 cm range when corrected for depth width. This mirrors the IPS which also slowly declined with depth from 0.164 to 0.104, while MI was over 0.99 and remained independent of depth.

Table 6: Process-based validation showing the root mean square of $Kink_{rms}$, $Energy_{rms}$, IPS and MI

Spline	Intervals	$Kink_{rms}$	$Energy_{rms}$	$Mismatch_{rms}$	IPS	MI
PhySpline	0-5 cm	0.000	0.493	0.000	0.164	0.998
	5-15 cm	0.000	0.409	0.000	0.136	0.999
	15-30 cm	0.000	0.391	0.000	0.130	0.998
	30-60 cm	0.000	0.378	0.000	0.126	0.999
	60-100 cm	0.000	0.359	0.000	0.120	0.998
	100-200 cm	0.000	0.314	0.000	0.104	0.996
C-SoftG	0-5 cm	0.004	0.191	1.478	0.557	0.992
	5-15 cm	0.004	0.153	1.227	0.461	0.975
	15-30 cm	0.004	0.150	1.293	0.482	0.942
	30-60 cm	0.004	0.140	1.245	0.463	0.921
	60-100 cm	0.005	0.128	1.212	0.450	0.922
	100-200 cm	0.003	0.107	1.395	0.501	0.941
C-EAS	0-5 cm	0.000	0.000	31.79	10.69	1.00
	5-15 cm	0.000	0.000	29.49	9.829	1.00
	15-30 cm	0.000	0.000	31.58	10.53	1.00
	30-60 cm	0.000	0.000	31.22	10.40	1.00
	60-100 cm	0.000	0.000	32.33	10.78	1.00
	100-200 cm	0.000	0.000	33.62	11.21	1.00

The composite IPS, integrating kink, energy and mismatch, decreased with depth from 0.165 in the 0–5 cm interval to 0.105 in the 100–200 cm layer, highlighting progressively lower structural penalties in deeper horizons. These patterns were consistent across more than 1.5 million horizon-level observations,

with the number of profiles per interval ranging from 140,031 (0–5 cm) to 610,964 (30–60 cm). The C-SoftG Kink ranged from 0.00334 at 100–200 cm to 0.00415 at 0–5 cm. The Energy decreased from 0.191 at 0–5 cm to 0.107 at 100–200 cm, whereas Mismatch remained elevated (1.22–1.47), reflecting less precise horizon alignment than phySpline. The depth-resolved IPS ranged from 0.451 at 60–100 cm to 0.557 at 0–5 cm. Profile counts matched those of phySpline, enabling direct comparison.

The C-EAS profiles showed minimal interfacial discontinuities (Kink $1.13–2.79 \times 10^{-16}$) and negligible internal roughness (Energy $\sim 10^{-29}$), but exhibited very large boundary misalignments (Mismatch 29.5–33.6), resulting in correspondingly high IPS values (9.83–11.2). Depth trends were relatively stable across intervals, with shallow layers (0–5 cm) showing slightly lower IPS than deeper horizons. The MI scores with harmonised depths follow that of the whole profile with all C-EAS having the highest MI followed by phySplines and C-SoftG.

3.2 Provincial scale

This visualisation approach required spatial analysis from the phySplines prior to implementation at the provincial scale. The spatial classification accuracy was approximately 50% across depth intervals, with a maximum of 54%. Similar spatial accuracies, despite good depth-function performance and realistic class distributions, have been reported previously (Flynn et al., 2024, 2022a). In this case, the spatial results were sufficient to support further profile-level analysis. Two transects, indicated by black and blue circles in the 0–5 cm layer and the black and blue transects (length ≈ 60–70 km) of the predicted classes (Figure 5), were therefore selected for visualisation of phySpline behaviour.

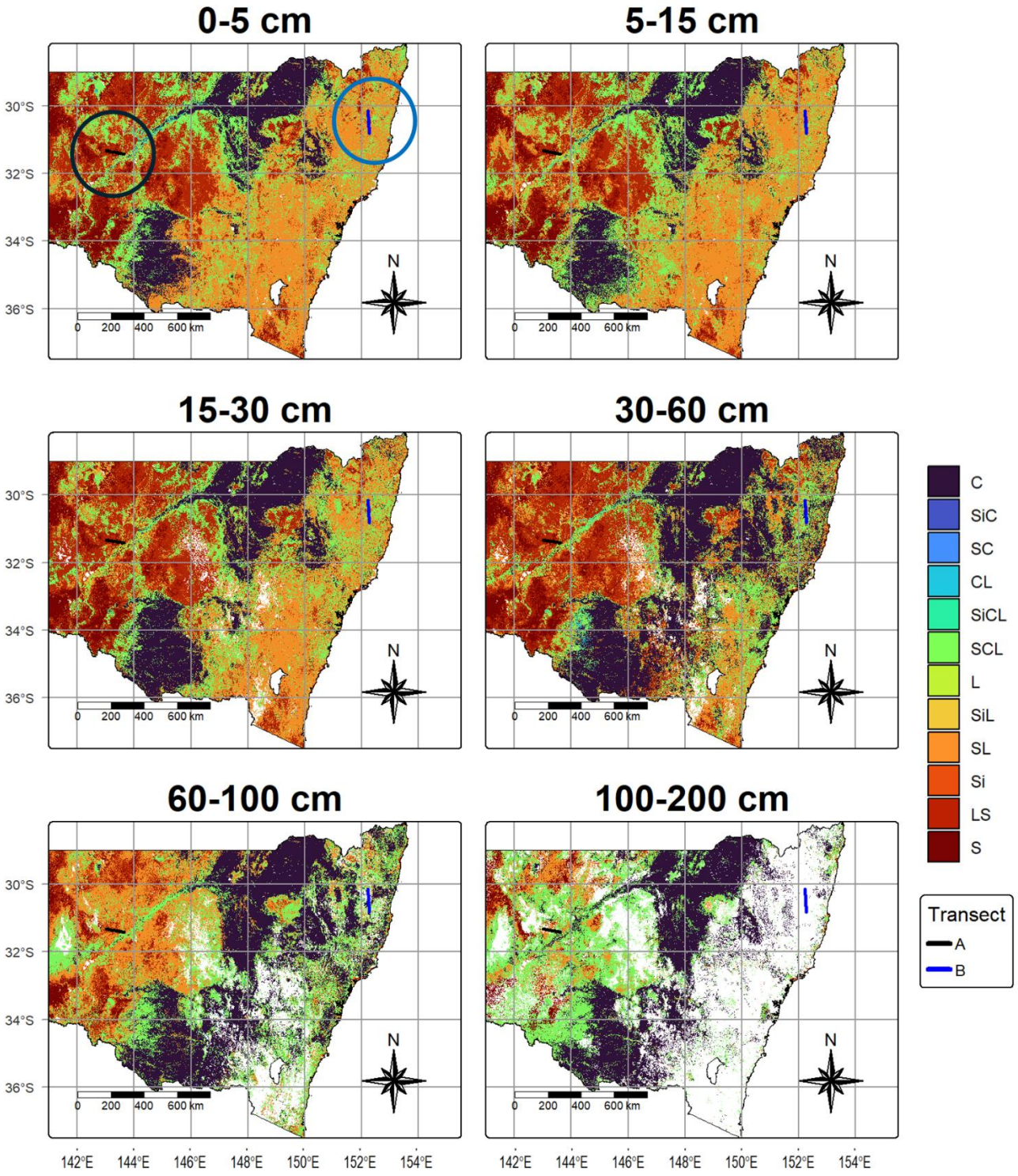

Figure 5: Predictions for New South Wales, Australia using phySpline harmonised texure classes as training data.

Both transects span approximately 60–70 km. Transect A is located in the semi-arid western region and runs west to east, while transect B traverses the more topographically variable, subtropical eastern region

from north to south. Transect A captures a higher number of pixels, providing finer spatial detail, whereas transect B covers a larger pixel area, resulting in a coarser but simplified visualisation. These transects illustrate differences in spatial resolution and visual representation across contrasting landscapes.

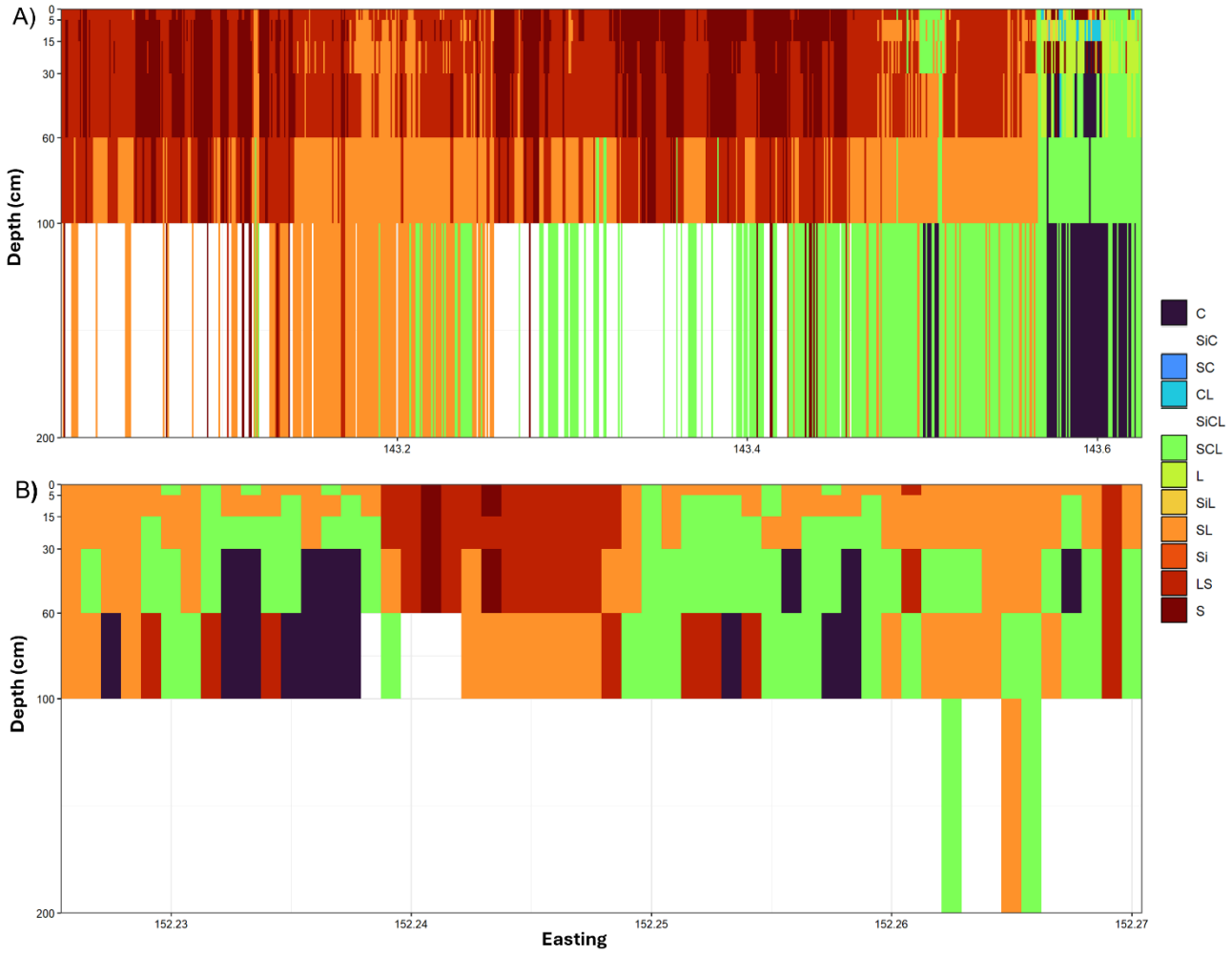

Figure 6: Cross sections used to display transects of the soil texture class (A) and each transect with depth intervals (B,C). The transects x-axis runs latitude or from west to east.

The provincial scale exhibited the greatest class imbalance (Table 7), with C occupying 40% of the dataset, yet it was underpredicted by less than 1.00% and remained with balanced predictions. In contrast, the spline overpredicted the SiC class, but only by 0.67% and misclassification decreased gradually away

from the dominant class in a systematic manner. Therefore, although the dataset was imbalanced, the predictions remained balanced and like the global scale.

Table 7: Confusion matrix for from phySplines interpolation on the WoSIS dataset in NSW, Australia.

	C	SiC	SC	CL	SiCL	SCL	L	SiL	SL	Si	LS	S	Recall
C	8665	343	32	3	1	0	0	0	0	0	0	0	0.96
SiC	0	52	4	1	0	0	0	0	0	0	0	0	0.91
SC	0	7	1122	52	2	1	0	0	0	0	0	0	0.95
CL	0	0	16	1060	24	2	0	0	0	0	0	0	0.96
SiCL	0	0	0	0	44	3	0	0	0	0	0	0	0.94
SCL	0	0	1	14	161	3786	56	6	0	0	0	0	0.94
L	0	0	0	0	1	19	919	3	1	0	0	0	0.97
SiL	0	0	0	0	0	1	7	75	0	0	0	0	0.90
SL	0	0	0	0	0	4	5	145	3707	8	0	0	0.96
Si	0	0	0	0	0	0	0	0	0	3	0	0	1.00
LS	0	0	0	0	0	0	0	2	7	78	1313	0	0.94
S	0	0	0	0	0	0	0	0	2	5	24	793	0.96
Precision	1.00	0.13	0.95	0.94	0.19	0.99	0.93	0.32	0.99	0.03	0.98	1.00	0.96

The Si class, despite its low prevalence, exhibited an apparent 100% accuracy, while most other classes achieved accuracies above 90%, except for SiC (86% accuracy). The high false positives can be seen in all the low prevalence classes of SiC (13%), SiCL (19%), SiL (32%) and Si (3%) which had an original prevalence of 0.25, 0.20, 0.37 and 0.01 in the dataset, respectively. Therefore, although the high accuracy of each class, the precision and recall give insight into the transition classes.

Class-resolved structural diagnostics revealed systematic, method-specific differences in spline performance (Figure 7). For phySpline, IPS values remained low across all classes (0.20–0.77), with

contributions dominated by internal energy rather than boundary discontinuities or boundary mismatches. The lowest IPS was observed for coarse loams (CL = 0.20), whereas the highest occurred in fine silty textures (Si = 0.77), reflecting slightly higher internal variation in these classes. C-SoftG exhibited moderate energy penalties coupled with substantial boundary mismatches (IPS ≈ 3–4.7), particularly in transitional textures such as SiL and SiC. In contrast, C-EAS displayed negligible Kink and energy penalties, but extreme boundary misalignments (IPS ≈ 6–17) across all classes, highlighting its perfect local fit at the expense of global structural fidelity.

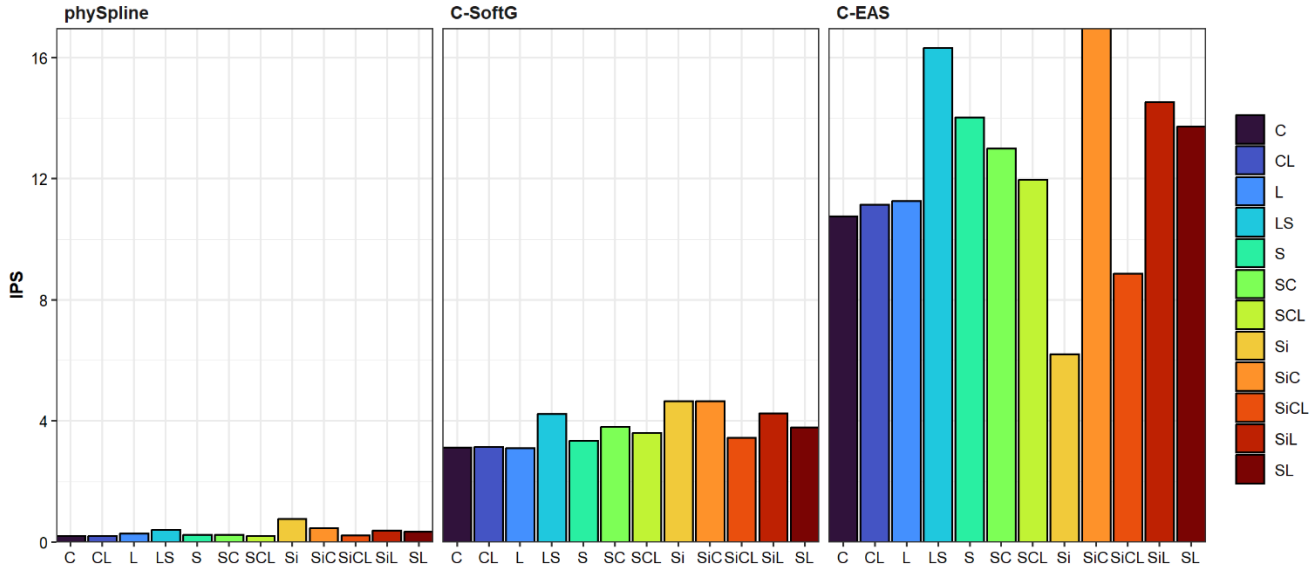

Figure 7: The Integral Process Score (IPS) for the C-EAS, C-SoftG and the phySpline for and its correspondence to each class.

3.3 Local scale

The Neno District dataset included 65 soil profiles with evenly represented soil texture classes (Figure 8). The only comparison with the reference splines was if the splines were over constrained with 0.00, 0.00 and 68.9 for the phySpline, C-SoftG and C-EAS, respectively. From these, six profiles were selected (Figure 2) for detailed analysis and overlaid with gridded environmental variables, including mean annual precipitation (MAP), mean annual temperature (MAT), elevation, slope, aspect and landform element (LFE). The selected profiles varied in depth, from shallow (Profile A, 35 cm) to deep (Profile F,

180 cm), and exhibited diverse texture patterns, ranging from shallow, coarse-textured profiles (Profile B, LS-SL, 35 cm) to deep, very fine textured soil (Profile E, SC-C, 150 cm). All profiles had low IPS of 0.10, 0.06, 0.05, 0.20, 0.03 and 0.04 for A, B, C, D, E, F and G, respectively.

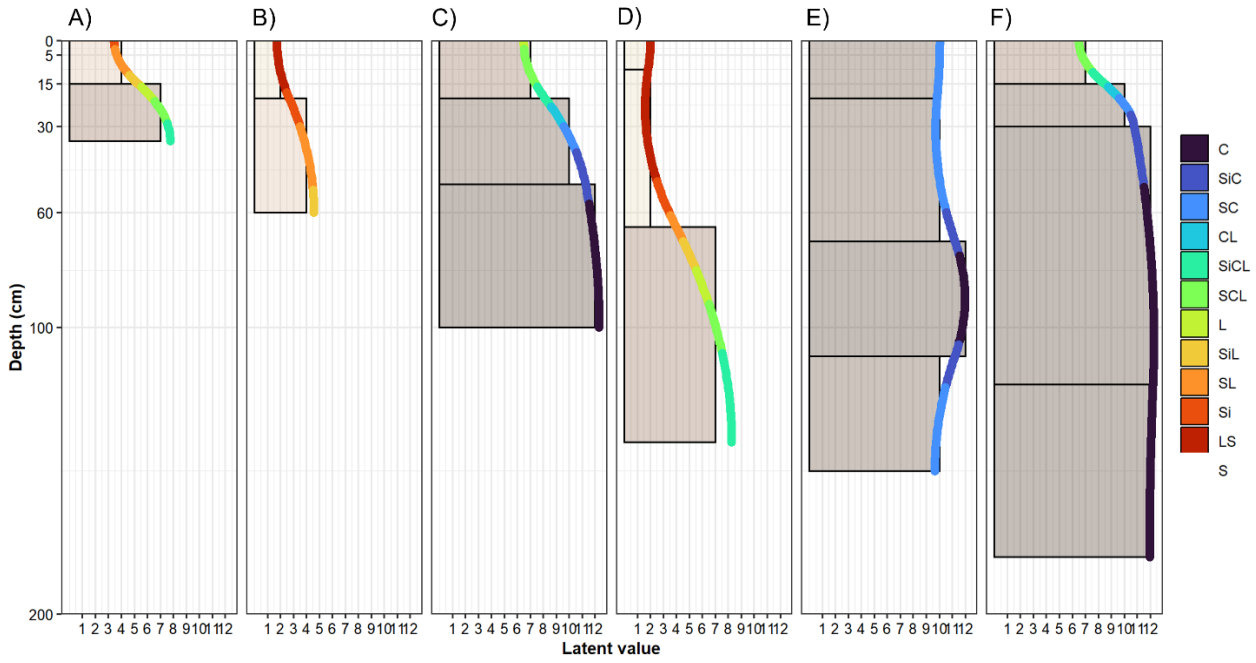

Figure 8: The selected profile's phySplines curve with their latent value on the y-axis to show how they correspond down the profile.

The selected profiles represented a broad spectrum of pedogenetic factors, requiring a model capable of adapting to diverse depth and texture patterns (Table 8). Environmental conditions across the site ranged from high-altitude, high-precipitation mountain slopes to low-relief, high-temperature depositional hollows. Profile F was located at 1,419 m elevation with high annual rainfall (96 mm) on a steep slope (15.1%), whereas Profile D was in a low-relief hollow (2.16% slope) with lower rainfall (76 mm) and higher mean annual temperatures (24 °C). Profiles A, B and C represent intermediate conditions on slopes and spurs, with slopes ranging from 4.47 to 9.60 degrees reflecting the steep topography of the Neno region.

Table 8: Environmental factors for each selected profile showing mean annual precipitation (MAP), mean annual temperature (MAT), elevation DEM, slope, aspect, landform element (LFE) and normalised mutual information per interpolated profile.

Profile	MAP (mm)	MAT (°C)	DEM (m)	Slope (%)	Aspect	LFE	MI
A	80	24	521.0	4.47	203	Slope	0.63
B	73	25	358.0	4.49	93.5	Spur	0.63
C	97	22	951.0	9.60	297	Slope	1.00
D	76	24	442.0	2.16	145	Hallow	0.58
E	95	20	1,261	16.7	50.5	Spur	0.51
F	96	19	1,419	15.1	119	Spur	0.95

The harmonised uncertainty profiles (Figure 9) provide a standardised measure of model confidence across soil horizons. These profiles capture uncertainty associated with the discrete depth intervals used in the phySpline solution, reflecting stability across harmonised depth intervals (Table 8). Uncertainty values appear to be largely independent of the phySpline curves and environmental factors. Thin layers exhibited both high and low uncertainty (e.g., A = 0.95, D = 0.03), while subsoil horizons (60–100 cm) also showed variable uncertainty (D = 0.75, E = 0.17). Profiles in contrasting landscape settings, such as

B in the Lisungwe valley with low rainfall and E in mountainous, steep terrain, displayed similar uncertainty patterns at 5–15 cm (B = 0.01, E = 0.04).

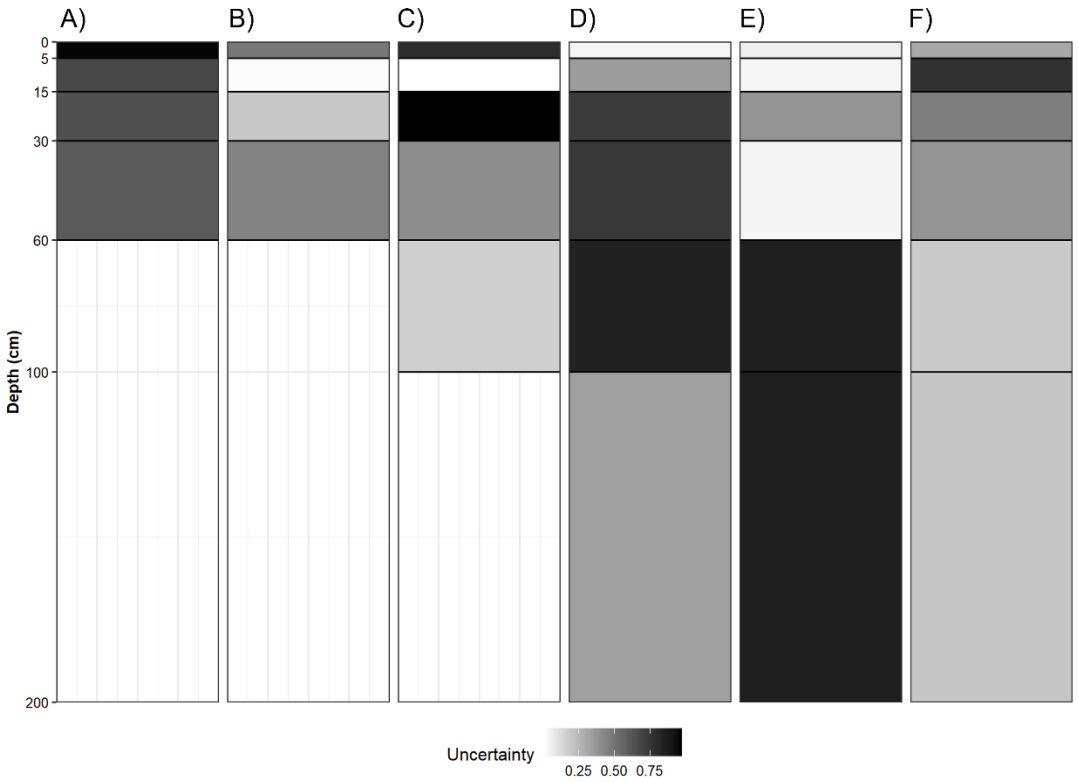

Figure 9: The uncertainties associated with the selected profiles shown for the harmonised soil depths.

Major classes with substantial observations, such as C, SC, SCL, SL, LS and S, were accurately predicted, showing recall values between 0.90 and 1.00. Some minor or sparsely represented classes (e.g., SiC, CL, SiCL, SiL, Si) had no observations in the test set, resulting in undefined recall and precision. Nevertheless, there were seven classes present in the dataset and 11 in the interpolated set. Yet misclassifications were minimal and mostly occurred between closely related classes, such as SC and SL, or SCL and L.

Table 9: Confusion matrix of the phySplines interpolation on the WoSIS dataset in the Neno District, Malawi.

	C	SiC	SC	CL	SiCL	SCL	L	SiL	SL	Si	LS	S	Recall
C	12	0	0	0	0	0	0	0	0	0	0	0	1.00
SiC	0	0	0	0	0	0	0	0	0	0	0	0	NA
SC	0	0	28	2	0	0	0	0	0	0	0	0	0.93
CL	0	0	0	0	0	0	0	0	0	0	0	0	NA
SiCL	0	0	0	0	0	0	0	0	0	0	0	0	NA
SCL	0	0	0	0	1	54	1	0	0	0	0	0	0.96
L	0	0	0	0	0	0	1	0	0	0	0	0	1.00
SiL	0	0	0	0	0	0	0	0	0	0	0	0	NA
SL	0	0	0	0	0	0	0	2	58	1	0	0	0.97
Si	0	0	0	0	0	0	0	0	0	0	0	0	NA
LS	0	0	0	0	0	0	0	0	0	1	49	0	0.98
S	0	0	0	0	0	0	0	0	0	0	0	3	100
Precision	1.00	0.00	1.00	0.00	NA	1.00	0.50	0.00	1.00	0.00	1.00	1.00	0.97

4 Discussion

Building on the foundation of previous work, we developed the phySpline: a categorical, physics-informed, and analytically solvable spline for interpolating soil classes with depth. The model is designed to capture pedological philosophy through gradient thresholds, where information is held in the form of potential energy within the soil profile, and resistance to change is governed by an Euler cumulative mass process. To illustrate its performance and novelty, we compared it against two reference spline: a modified equal-area spline capable of classification (C-EAS) and an intermediate spline incorporating a continuity matrix (C-SoftG). The splines were evaluated using the WoSIS dataset at global, provincial (NSW, Australia), and local (Neno District, Malawi) scales. Validation considered both statistical performance and physical realism to determine whether the observed spline behaviour reflected genuine pedological patterns or merely mathematical coincidences. This multi-scale evaluation highlights the ability of the phySpline to maintain process-based continuity, structural fidelity, and pedological interpretability across diverse soil environments.

4.2.1 Spline performance and lambda

Across all spatial supports, phySplines exhibited a consistent and interpretable relationship between the regularisation parameter λ_r, predictive accuracy, kappa and RMSE (Table 2). Decreasing λ_r systematically increased overall accuracy and agreement while reducing RMSE, demonstrating that λ_r functions as a physically meaningful process-based control rather than a purely statistical tuning parameter. At the global scale, an 80% reduction in λ_r (0.50 - 0.10) produced a disproportionate improvement in model performance (kappa $\approx$ 0.66 - 0.93; RMSE $\approx$ 0.37 - 0.13), whereas further reductions yielded diminishing returns. This clear inflection supported the use of the elbow criterion to identify λ_r = 0.10 as the optimal point that balanced fidelity and generalisation.

The phySplines framework demonstrated exceptional numerical stability, maintaining structural integrity even when λ_r was reduced to 1.0×10^{-5}. Unlike traditional splines, which typically exhibit erratic "hooking" or oscillatory behaviour at low smoothing levels, phySplines remained physically consistent. This stability is attributed to the Euler cumulative mass process, where depth-dependent resistance (e^{kz}) acts as an internal physical damper.

By prioritising the exact analytic integral of the mass reservoirs over pointwise midpoint estimates, the model achieved kappa values of 0.94–0.96 without over-constraining the solution. The high fidelity to horizon observations does not result in a "staircase" effect; instead, the minimisation of the weighted Jacobian energy ensures that transitions between texture classes are represented as continuous gradients. This allows for the capture of transitional states (the latent taxonomic shifts between horizons) that are often lost in discrete classification or over-smoothed continuous models.

4.2.2 Physics-informed, process-based and self-regularised

The intent of the reference functions was not for benchmarking but to contextualise the progression from purely statistical splines to a physics-informed, process-based formulation. While accuracy metrics alone

suggest broadly comparable performance at $\lambda_r < 0.10$, this can mask fundamental differences in structural behaviour (Table 3). PhySplines uniquely enforced continuity through a null-space projection and the integrals used, yielding exact slopes (zero kink, C^1), exact values (zero mismatch, C^0), horizon boundaries space ($z \in [0, 1]$), and smooth internal curvature simultaneously. This contributed to low internal potential energy and high mutual information, producing a physically realistic spline with strong and independent class resolve. Even when horizons appeared visually discrete, maintaining mass continuity when interpolating or harmonising to new depth intervals was critical, as it preserved the integrity of pedogenic transitions and ensured that derived thresholds reflected the underlying, physically coherent soil structure in unsampled locations (Table 4). The phySpline remained unconstrained for all scales.

By contrast, the C-EAS achieved perfect local fits by construction but oversimplified profile structure and suppressed transitional behaviour, resulting in extreme boundary mismatches at the profile scale (high IPS and MI). This produced splines that were statistically enhanced but physically implausible, effectively overfitting the data at the expense of continuity and was over-constrained for all scales. Nevertheless, it reflects the philosophical view that soil classes are inherently discrete and may carry limited physical meaning, a perspective of conceptual significance. The C-SoftG remained unconstrained, with a moderate IPS and MI, allowed smoother transitions but sacrificed derivative continuity and boundary alignment. PhySplines were the only approach to resolve these trade-offs explicitly, embedding soil-process realism directly into the analytical solution rather than relying on post hoc constraints.

Although MI was relatively high across all splines, Figure 3A demonstrates that phySplines maintained continuity in both depth and latent space without disconnects between transitions. Visually, this indicates that when harmonising soil texture classes, phySplines correctly integrate over the new depth interval. Figure 3B and 3C illustrate latent value mismatches for C-SoftG and C-EAS, highlighting structural

617 divergence despite high numerical accuracy. Figure 3E shows the clear stability effect phySplines
618 pseudo-horizon had on the coefficients, while Figure 3F demonstrated the clear need to impute the
619 median. Unexpectedly, C-EAS transitions between classes without knowledge of a horizon, a behaviour
620 the deserves further investigation

621 These findings indicate that phySplines reconstruct vertically coherent soil profiles consistent with
622 pedogenic theory, reframing depth functions as minimising the potential energy of the soil profile through
623 the exact integral of the cumulative mass. By uniting visual fidelity, physical plausibility and categorical
624 integrity, phySplines provide a fully interpretable framework to see between horizons, capturing both
625 subtle and abrupt pedogenetic transitions in a continuous, process-informed manner.

626 ### 4.2.3 Global scale: process realism and depth-structured soil behaviour

627 Having established that phySplines respond to regularisation in a scale-independent and physically
628 interpretable manner, the global-scale results demonstrated how this behaviour translated into
629 pedologically realistic depth structure. At this extent, phySplines maintained stable class behaviour
630 despite moderate imbalance in class frequencies (Table 5). Dominant texture classes were not amplified,
631 while rare classes were retained as meaningful components of the latent process space rather than
632 suppressed or absorbed. Misclassifications occurred primarily among neighbouring texture classes,
633 reflecting transitional uncertainty rather than categorical failure. This behaviour is consistent with
634 pedological expectations, where soil texture transitions were gradual and classes represent discretised
635 interpretations of the underlying continuum.

636 Depth-resolved behaviour further supported this interpretation. A systematic vertical organisation of
637 texture classes emerged across class domain, with finer textures preferentially expressed at depth and
638 coarser or loamy textures concentrated near the surface (Figure 4). The C, SiC, and SC classes exhibited
639 signs of illuviation around 60 cm and remained stable through the remainder of the profile, whereas SiL

and SL followed the opposite trend. Nevertheless, these overall patterns aligned with established pedological processes such as eluviation–illuviation, residual enrichment, and cumulative weathering (Buol et al., 2011; Jenny, 1941). These trends were recovered without explicit depth stratification or class-specific constraints. Mutual information remained high and independent of depth, exceeding 0.99 across all harmonised intervals, indicating strong class fidelity, while C-SoftG exhibited decreasing values with depth, suggesting reduced structural coherence in deeper horizons.

Uncertainty was not associated with depth-related class behavior; it neither tracked class-specific depth trends nor displayed an independent, quantifiable trend with depth. However, they were also independent of number of observations, making it challenging to interpret and seemingly decoupled from the system. However, these uncertainty estimates provide useful contextual information within the harmonised dataset. For example, the Si class exhibited relatively more and consistent uncertainty at the global scale than any other classes, or we can be 60% certain that the interpolations are Si from 15 – 60 cm. This is also where SL and LS, the neighboring classes start to decline and were Si reaches its uncertainty plateau.

This structure arises from the physics-informed, energy-minimising formulation of phySpline (Table 6). From top to bottom, energy gradually declines with depth, reflecting measurable structural variability. Given the model's numerous constraints and limited degrees of freedom, the absolute energy is expected to exceed that of reference groups. Cumulative mass weighting progressively stiffens the spline with depth, allowing greater variability and thus higher energy near the surface while suppressing unrealistic oscillations in deeper horizons, a limitation previously noted for equal-area splines below discrete transitions (Odgers et al., 2012). The depth-resolved behavior reconstructed by phySpline aligns with classical pedological concepts: horizon boundaries act as conceptual thresholds rather than abrupt physical breaks (Schaetzl and Thompson, 2015). By preserving continuous gradients and minimising rather than eliminating energy, phySpline retains information lost in purely geometric approaches (e.g., C-EAS) and accurately represents the vertical integration of pedogenic processes.

664 At the global scale, phySpline demonstrates strong generalization, as evidenced by the consistent overall
665 trend, decoupled uncertainties, and the energy-minimising regularisation term. These features indicate
666 that the method reliably captures soil structural patterns while preserving physically meaningful gradients
667 across diverse landscapes.

668 ### 4.2.4 Provincial scale: spatial heterogeneity and profile coherence

669 Spatial analysis along with transect views of the phySplines were incorporated into the province scale
670 analysis. Spatial classification accuracy ranged from approximately 50 to 54% across depth intervals,
671 which was considered sufficient to support profile-level interpretation as it was consistent to other studies
672 (Chaney et al., 2016; Radočaj et al., 2023; Sabbaghi et al., 2024) for depth-function–based soil mapping
673 using national and continental scale maps (Bodenstein et al., 2022; Feeney et al., 2022; Simperegui et
674 al., 2025) with the high degree of vertical accuracy 96%.

675 The spatial prediction served primarily as a vehicle for assessing profile-scale behaviour across
676 contrasting landscapes (Figure 5) and the transects show the lateral view (Figure 6). The predicted maps
677 reflect various soil-forming processes across the province, ranging from aeolian deposits with deep S
678 enriched Psamments (Kandosols) and Calcids (Calcarasols) in the west supporting livestock. Deep C rich
679 Vertisols follow mafic/ultra-mafic parent material and the saline basins of the Murry-Darling Basin
680 network (Gray et al., 2016). Illuviation occurs with C accumulation around 30 to 60 cm on the stable
681 rolling hills of the western slopes in highly fertile Alfisols (Chromosols) supporting various crops (Scott
682 et al., 2007). The progression continues into the high-energy erosional regimes of the Eastern Highlands,
683 which are characterised by fluctuating soil states and types, and finally to the dynamic alluvial deposition
684 of the floodplains (Pain et al., 2011; Searle, 2021).

685 The transect visualisations are a great tool for environmental models with their essential movement from
686 the academic to the public domain where clear communication and visualisation are critical (Dahlstrom,

2014; Pandey et al., 2014; Vereecken et al., 2016). Smooth, laterally coherent depth transitions were maintained across both transects despite strong contrasts in visualisation techniques, soil type and landscape position. The transects reflect what was seen in the two-dimensional maps and help visualise the more realistic multi-dimensional state of soil where three-dimensional soil mapping is becoming more important (Lin et al., 2025). Therefore, with this knowledge and visualisation method, it becomes viable not only to interpolate unseen classes but also to predict and visualise unseen profiles based on soil types or geomorphic patterns using the framework from Wiese et al. (2016).

Despite pronounced class imbalance, dominant textures such as C remained stable and were underpredicted by less than 1% (Table 7), while low-prevalence classes such as SiC, SiCL and SiL were overpredicted by small margins of 0.67% or less. Misclassifications occurred systematically among adjacent texture classes, reflecting transitional uncertainty rather than failure to capture dominant textures and was not a result of class numbers. Class-resolved structural diagnostics corroborated these findings (Figure 7). Integrated process scores remained low across all texture classes (0.20–0.77), with contributions dominated by internal curvature rather than boundary mismatches or boundary discontinuities. Transitional textures exhibited slightly higher internal energy, consistent with their pedological role as intermediate textures rather than discrete endmembers. This indicates that the model complexity is concentrated on resolving the fluid gradients between these textural poles rather than correcting for mathematical inconsistencies at the horizon interfaces.

The province scale showed the visualisation power of classification and the predictions closely followed the spatial patterns of NSW lithology maps (Gray et al., 2016) and Australian soil classification map (Malone et al., 2025). While this correspondence is expected due to shared environmental covariates, phySpline reproduces these patterns through a physics-informed framework, rather than explicit spatial tuning. This suggests that spatial soil class predictions can be interpreted as expressions of underlying

potential energy gradients and self-regularisation of Euler's cumulative mass process, an implication that warrants further investigation.

4.2.5 Local scale: linking spline behaviour to pedogenetic processes

At the local scale, the phySpline facilitated direct interpretation of soil-forming processes by integrating depth-continuous predictions with environmental covariates. The Neno District dataset included 65 soil profiles with well-represented soil texture classes, from which six profiles were selected for detailed analysis across a range of slopes, elevations, precipitation regimes and landform elements (Figure 8; Figure 2). Selected profiles varied in depth from 35 to 180 cm and encompassed shallow, coarse-textured soil (LS-SL) to a deep, fine-textured soil (SC-C).

In many profiles, additional interpolated texture classes emerged (11 classes) relative to the original observations (7 classes), reflecting the spline's ability to resolve transitional states that are typically unobserved yet pedologically plausible. This highlights the complexity of categorical transitions often overlooked by conventional models and demonstrates that these transitions can be captured deterministically and analytically, without relying on fuzzy-set approaches. Most profiles exhibited systematic enrichment in finer particles with depth, consistent with percolation-driven clay translocation processes such as lessivage.

Different topography, precipitation, temperature and slope position all reflect the differences in the profiles seen (Table 8). Nevertheless, it was thought that geology, vegetation and time were the main environmental factors contributing to the pattern of soil patterns seen, factors that are more difficult to examine due to timescales and dynamics. In the Neno mountain region, stabilising vegetation enhanced water infiltration and reduced surface runoff, thus promoting clay accumulation in the upper subsoil, consistent with previous findings on soil–vegetation interactions on mafic substrates (De Baets et al., 2006; Gyssels et al., 2005).

Particularly in profiles C and F, these were interpretable in terms of lateral water movement and landscape position rather than vertical drainage, both showing a pronounced clay increase around 10–15 cm. This reflects downslope translocation of clay influenced by steep slopes (>9%), where erosion has depleted the topsoil, exposing the clay-rich subsoil. Profile E was found in a similar location but with a slope of 16%, and it was inferred that erosion had completely removed the topsoil. Profiles A, B, and D are located in the Lisungwe Valley on sloping positions with light textures (LS–SL), where water moves predominantly vertically on spur, slope, and hollow positions. Profile D is deeper, most likely due to the accumulation potential of hollows, as it is a concave slope, unlike a spur, which is a convex slope.

Profiles A, B and D overshot their endmember classes; however, this occurred in a mass-conservative manner and resulted in representations that were more pedologically realistic than solutions constrained to remain strictly within class bounds. Profiles C and F did not overshoot their endmembers and were initially consistent with expected pedological structure. However, Profile F required the center of mass to be shifted toward the top of the horizon to achieve a more realistic representation.

These observations are particularly important for depth harmonisation, as they demonstrate that uncertainty patterns were largely decoupled from continuous interpolations. This indicates that the imposed boundary constraints maintained numerical stability and continuity, while mitigating limitations previously associated with drift effects. The partial independence between uncertainty estimates and interpolated class assignments gives phySpline distinct practical and conceptual utility. Whereas high uncertainty is often interpreted as misclassification or insufficient sample support, in phySpline uncertainty is directly proportional to proximity to a class transition. In the Neno District, classifications were largely correct, and elevated uncertainties consistently reflected transitional states rather than model failure, indicating a measure that can be meaningfully used in practice without complexity.

4.2.6 Transferability, data requirements and limitations

The consistent performance of phySpline across global, provincial, and local scales demonstrates its robustness and transferability beyond the regions explicitly evaluated. Unlike purely data-driven classifiers, phySplines are governed by the information by self-regularisation and minimising the potential energy, making predictions independent of spatial support or sample size. Consequently, variations in observation density do not compromise structural integrity or class transitions. Comparable accuracy, class balance, and process-based diagnostics were observed in both sparsely sampled regions (e.g., NSW) and densely sampled regions (e.g., Neno), despite differences in sampling density, landscape heterogeneity, and soil moisture regimes.

At minimum, phySplines require vertically ordered soil horizon observations with defined depth intervals and categorical texture assignments. The method tolerates missing horizons through controlled extrapolation, but at least two observed horizons are required to anchor the latent process curve. Each profile is solved independently, so performance is driven by the number and quality of profiles rather than spatial sampling density. Where not all texture classes are observed, phySplines can be informed that additional classes are permissible, allowing transitional classes to emerge naturally along the latent curve. Where latent ordering is not apparent (e.g., numerical classification) can be arranged according to physically meaningful attributes, such as diagnostic horizon moisture, drainage class or Munsell color. Importantly, unlike over-constrained spline formulations (e.g., C-EAS), phySplines do not become over-constrained, meaning additional constraints can be applied without compromising the solution.

Performance may degrade when profiles are extremely shallow and abrupt horizons, lack reliable vertical ordering or include inconsistently defined texture classes across surveys. Limitations inherent to taxonomic classification may influence spline performance. In soil science, C, Si and S are commonly measured and combined to define texture classes. Except for C, neither S nor Si represent dominant

778 classes or display systematic depth-dependent transitions at any scale, reflecting their limited influence
779 on profile structure. This may arise from the specific USDA diagnostic dimensions used (S = 0.05–2.0
780 mm; Si = 0.002–0.05 mm) or from the GlobalSoilMap standard depth intervals. Prior studies have
781 similarly noted that conventional taxonomic systems may be unable to fully capture their functional roles
782 (Duniway et al., 2013; Hartemink, 2015; Morrow, 2023; Vigués Jorba et al., 2025). Consequently, the
783 depth intervals may have either highlighted this limitation, contributed to its manifestation in the dataset
784 or the soil texture classification did.

785 Future improvements could incorporate probabilistic uncertainty via Bayesian or Monte Carlo methods.
786 While current deterministic interpolations are easily interpretable and support endmember
787 reconstruction, probabilistic approaches could enhance risk assessment or climate-change modeling.
788 Although the algorithm is computationally efficient (~101,568 profiles in <9 min), large raster datasets
789 will require further optimisation, such as parallelisation or implementation on platforms like Google
790 Earth Engine, building on recent advances in grid-based (Flynn et al., 2024). The phySpline framework
791 could be extended to a multinomial or multi-dimensional latent space, allowing it to capture complex
792 inter-class transitions while remaining physics-informed and interpretable, though adoption depends on
793 acceptance of this multidimensional perspective.

794 4.2.7 Implications for taxonomic information and pedometrics

795 In practice, phySplines transform what was once a computational and conceptual bottleneck into a fully
796 continuous, analytically tractable framework. By resolving chronic profile boundary instabilities and
797 complex categorical transitions found in traditional splines, they maintain pedological realism through a
798 system that is mass-conservative, energy minimising, self-regularising and analytically solvable. Their
799 ability to handle class imbalances and remain transferable across diverse sampling densities opens the
800 way for next-generation soil profile modelling. Ultimately, phySplines demonstrate that the complex

transitions inherent to pedological philosophy hold untapped potential for soil thermodynamic multifunctionality; by quantifying these gradients, the framework converts static taxonomic observations into a dynamic, interpretable story of the vertical soil continuum. This provides researchers, policymakers and environmental models with a framework to meaningfully visualise and understand soil complexity.

PhySplines employ the exact analytic integral of the Euler cumulative resistance process, which integrates stiffness continuously across the full horizon thickness. This shift eliminates the "midpoint trap," ensuring that both boundary and interior behaviour are informed by the actual distribution of mechanical and structural resistance. By capturing the continuous cumulative effect of depth-dependent stiffness, the method preserves physically consistent curvature, maintains exact horizon continuity and allows boundary conditions to emerge naturally. The result is a fully physics-informed, analytically tractable spline that represents the horizon as a continuous process rather than a discrete approximation, providing a realistic profile view that is not over-constrained.

Crucially, this framework bridges the gap between taxonomic nomenclature and physical laws: categorical shifts are treated as high-fidelity indicators of pedogenetic change. Traditional, over-constrained numerical splines are replaced with a physics-informed, flexible system that respects both soil processes and mathematical rigour. This approach captures complex landscape trends within a deterministic framework, mimicking the experience of traversing a terrain where environmental gradients blend seamlessly into distinct soil classes. By resolving previously unmodelled transitions, phySplines preserve taxonomic fidelity without sacrificing mathematical precision, offering a visually accurate and interpretable way to “see” between horizons.

Conclusion

This study introduced phySpline, a physics informed, analytically solvable spline for interpolating categorical soil classes across depth. By embedding pedological philosophy including continuity whether gradual or virtually discrete and horizon boundary constraints into a fully continuous and differentiable framework, phySpline captures both observed and previously unmodeled transitional states, preserving process-based gradients that reflect real soil processes. Across global, provincial and local scales, phySpline achieved high classification accuracy while maintaining mass preservation, potential energy minimisation and pedological fidelity within a deterministic model. By bridging soil texture classes and exact integrals, phySpline maintains interpretability and supports effective communication within a mathematically robust framework. By resolving complex transitions and anchoring profile terminals, phySpline transforms discrete, human-assigned classes into continuous, physically meaningful representations. Future applications should extend this framework to multinomial and continuous properties, establishing a multifunctional platform that integrates physics-informed constraints with data-driven modeling to advance a new paradigm for profile-level soil interpolations and multi-disciplinary interpretations.

References

Amundson, R., Sanderman, J., Yoo, K., Chitsaz, M., Abramova, A., Georgiou, K., 2025. Neglecting vertical transport leads to underestimated soil carbon dynamics. Nat. Geosci. 18, 1239–1244. https://doi.org/10.1038/s41561-025-01846-6

Araya, Y.N., Emmott, A., Rawes, W., Zuza, E.J., 2023. Promoting climate-smart sustainable agroforestry to tackle social and environmental challenges: The case of macadamia agroforestry in Malawi. Journal of Agriculture and Food Research 14, 100846–100846. https://doi.org/10.1016/j.jafr.2023.100846

ASRIS, 2024. ASRIS - Australian Soil Resource Information System.

Australian Bureau Of Meteorology, 2019. Australian Gridded Climate Data (AGCD).

Basu, S., Isik, M.U., 2020. Categorical Complexity. Forum of Mathematics, Sigma. https://doi.org/10.48550/ARXIV.1610.07737

Benbi, D.K., Toor, A.S., 2026. Spatial and Depth Distribution of Soil Carbon and Nitrogen in Relation to Agricultural Management, Climate and Textural Control on Carbon Sequestration Potential. Communications in Soil Science and Plant Analysis 57, 248–267. https://doi.org/10.1080/00103624.2025.2589768

Bishop, T.F.A., McBratney, A.B., Laslett, G.M., 1999. Modeling soil attribute depth functions with equal-area quadratic smoothing splines. Geoderma 91, 27–45. https://doi.org/10.1016/S0016-7061(99)00003-8

Blewett, ichard (Ed.), 2012. Shaping a Nation: A Geology of Australia. ANU Press. https://doi.org/10.22459/SN.08.2012

Bodenstein, D., Clarke, C., Watson, A., Miller, J., Van Der Westhuizen, S., Rozanov, A., 2022. Evaluation of global and continental scale soil maps for southern Africa using selected soil properties. CATENA 216, 106381. https://doi.org/10.1016/j.catena.2022.106381

Bortolus, A., 2008. Error Cascades in the Biological Sciences: The Unwanted Consequences of Using Bad Taxonomy in Ecology. AMBIO: A Journal of the Human Environment 37, 114–118. https://doi.org/10.1579/0044-7447(2008)37%255B114:ECITBS%255D2.0.CO;2

Buol, S.W., Southard, R.J., Graham, R.C., McDaniel, P.A., 2011. Soil Genesis and Classification, 1st ed. Wiley. https://doi.org/10.1002/9780470960622

Burrough, P.A., Van Gaans, P.F.M., Hootsmans, R., 1997. Continuous classification in soil survey: Spatial correlation, confusion and boundaries. Geoderma 77, 115–135. https://doi.org/10.1016/S0016-7061(97)00018-9

869 Chaney, N.W., Wood, E.F., McBratney, A.B., Hempel, J.W., Nauman, T.W., Brungard, C.W., Odgers,
870 N.P., 2016. POLARIS: A 30-meter probabilistic soil series map of the contiguous United States.
871 Geoderma 274, 54–67. https://doi.org/10.1016/j.geoderma.2016.03.025
872 Cheng, C., Messerschmidt, L., Bravo, I., Waldbauer, M., Bhavikatti, R., Schenk, C., Grujic, V., Model,
873 T., Kubinec, R., Barceló, J., 2024. A General Primer for Data Harmonization. Sci Data 11, 152.
874 https://doi.org/10.1038/s41597-024-02956-3
875 Cohen, J., 1960. A Coefficient of Agreement for Nominal Scales. Educational and Psychological
876 Measurement 20, 37–46. https://doi.org/10.1177/001316446002000104
877 Colwell, J.D., 1970. A statistical-chemical characterization of four great soil groups in Southern New
878 South Wales based on orthogonal polynomials. Soil Research 8, 221–238.
879 CSIRO, 2024. Australian Soil Resource Information System Website. Data Collection.
880 Dahlstrom, M.F., 2014. Using narratives and storytelling to communicate science with nonexpert
881 audiences. Proc. Natl. Acad. Sci. U.S.A. 111, 13614–13620.
882 https://doi.org/10.1073/pnas.1320645111
883 De Baets, S., Poesen, J., Gyssels, G., Knapen, A., 2006. Effects of grass roots on the erodibility of topsoils
884 during concentrated flow. Geomorphology 76, 54–67.
885 https://doi.org/10.1016/j.geomorph.2005.10.002
886 Duniway, M.C., Miller, M.E., Brown, J., Toevs, G., 2013. An alternative to soil taxonomy for describing
887 key soil characteristics. Frontiers in Ecol & Environ 11, 527–528.
888 https://doi.org/10.1890/13.WB.020
889 Feeney, C.J., Cosby, B.J., Robinson, D.A., Thomas, A., Emmett, B.A., Henrys, P., 2022. Multiple soil
890 map comparison highlights challenges for predicting topsoil organic carbon concentration at
891 national scale. Sci Rep 12, 1379. https://doi.org/10.1038/s41598-022-05476-5
892 Fick, S.E., Hijmans, R.J., 2017. WorldClim 2: new 1km spatial resolution climate surface for global land
893 areas. International Journal of Climatology 37, 4302–4315.

Flynn, T., de Clercq, W., Rozanov, A., Clarke, C., 2019. High-resolution digital soil mapping of multiple soil properties: an alternative to the traditional field survey? South African Journal of Plant and Soil 1–11. https://doi.org/10.1080/02571862.2019.1570566

Flynn, T., Kostecki, R., Rebi, A., Raza, T., 2024. Accessing global soil raster images and equal-area splines to estimate soil organic carbon stocks on the regional scale. Pedosphere S1002016024000699. https://doi.org/10.1016/j.pedsph.2024.07.004

Flynn, T., Rozanov, A., Ellis, F., de Clercq, W., Clarke, C., 2022a. Farm-scale digital soil mapping of soil classes in South Africa. South African Journal of Plant and Soil. https://doi.org/10.1080/02571862.2022.2059115

Flynn, T., Wiese, L., Rozanov, A., 2022b. Soil carbon stock assessment using depth and spatial models on afforested arable lands. South African Journal of Plant and Soil 1–13. https://doi.org/10.1080/02571862.2022.2079741

Gray, J.M., Bishop, T.F.A., Wilford, J.R., 2016. Lithology and soil relationships for soil modelling and mapping. CATENA 147, 429–440. https://doi.org/10.1016/j.catena.2016.07.045

Gyssels, G., Poesen, J., Bochet, E., Li, Y., 2005. Impact of plant roots on the resistance of soils to erosion by water: a review. Progress in Physical Geography: Earth and Environment 29, 189–217. https://doi.org/10.1191/0309133305pp443ra

Hartemink, A.E., 2015. The use of soil classification in journal papers between 1975 and 2014. Geoderma Regional 5, 127–139. https://doi.org/10.1016/j.geodrs.2015.05.002

Hastie, T., Tibshirani, R., Friedman, J., 2009. The Elements of Statistical Learning, 2nd ed. Springer Series in Statistics.

Henderson, M.M., Serences, J.T., Rungratsameetaweemana, N., 2025. Dynamic categorization rules alter representations in human visual cortex. Nat Commun 16, 3459. https://doi.org/10.1038/s41467-025-58707-4

Hillebrand, H., Blasius, B., Borer, E.T., Chase, J.M., Downing, J.A., Eriksson, B.K., Filstrup, C.T., Harpole, W.S., Hodapp, D., Larsen, S., Lewandowska, A.M., Seabloom, E.W., Van De Waal, D.B., Ryabov, A.B., 2018. Biodiversity change is uncoupled from species richness trends: Consequences for conservation and monitoring. Journal of Applied Ecology 55, 169–184. https://doi.org/10.1111/1365-2664.12959

Hillel, D., 1998. Environmental Soil Physics, Journal of Environment Quality. Academic Press, San Diego, CA. https://doi.org/10.2134/jeq1999.00472425002800060046x

Isaac, N., 2004. Taxonomic inflation: its influence on macroecology and conservation. Trends in Ecology & Evolution 19, 464–469. https://doi.org/10.1016/j.tree.2004.06.004

ISRIC, 2021. World Soil Information Service (WoSIS). ISRIC - World Soil Information.

Jenny, H., 1941. Factors of Soil Formation: A System of Quantitative Pedology. McGraw- Hill, NY. https://doi.org/10.2307/211491

Kempen, B., Brus, D.J., Stoorvogel, J.J., 2011. Three-dimensional mapping of soil organic matter content using soil type-specific depth functions. Geoderma 162, 107–123.

Kienast-Brown, S., Philippe, J., Nauman, T., Libohova, Z., Roecker, S., Thompson, J., 2021. Comparison of Spline Depth Interval and Point-Depth Approaches for Predicting Soil Properties. Presented at the 2021 NCSS (National Cooperative Soil Survey) National Conference., USDA-NRCS.

Kleidon, A., 2010. Life, hierarchy, and the thermodynamic machinery of planet Earth. Physics of Life Reviews 7, 424–460. https://doi.org/10.1016/j.plrev.2010.10.002

Kuhn, M., Johnson, K., 2013. Applied Predictive Modeling. Springer New York. https://doi.org/10.1007/978-1-4614-6849-3

Leewis, M.-C., Lawrence, C.R., Schulz, M.S., Tfaily, M.M., Ayala-Ortiz, C.O., Flores, G.E., Mackelprang, R., McFarland, J.W., 2022. The influence of soil development on the depth distribution and structure of soil microbial communities. Soil Biology and Biochemistry 174, 108808. https://doi.org/10.1016/j.soilbio.2022.108808

Lin, Z., Xu, J., Lu, M., 2025. Enhanced three-dimensional mapping of soil texture components using quantile regression forest and spline techniques in Jiangsu Province, China. Sci Rep 16, 1646. https://doi.org/10.1038/s41598-025-31144-5

Ma, Y., Condon, L.E., Koch, J., Bennett, A., Defnet, A., Tijerina-Kreuzer, D., Melchior, P., Maxwell, R.M., 2026. High resolution US water table depth estimates reveal quantity of accessible groundwater. Commun Earth Environ 7, 45. https://doi.org/10.1038/s43247-025-03094-3

Malone, B., Searle, R., 2022. Soil and Landscape Grid National Soil Attribute Maps - Sand (3" resolution) - Release 2. https://doi.org/10.25919/RJMY-PA10

Malone, B.P., McBratney, A.B., Minasny, B., Laslett, G.M., 2009. Mapping continuous depth functions of soil carbon storage and available water capacity. Geoderma 154, 138–152. https://doi.org/10.1016/j.geoderma.2009.10.007

Malone, B.P., Searle, R., Stenson, M., McJannet, D., Zund, P., Román Dobarco, M., Wadoux, A.M.J.-C., Minasny, B., McBratney, A., Grundy, M., 2025. Update and expansion of the soil and landscape grid of Australia. Geoderma 455, 117226. https://doi.org/10.1016/j.geoderma.2025.117226

McDougall, K.L., Hardy, G.E.S.J., Hobbs, R.J., 2002. Distribution of Phytophthora cinnamomi in the northern jarrah (Eucalyptus marginata) forest of Western Australia in relation to dieback age and topography. Australian Journal of Botany 50, 107–107. https://doi.org/10.1071/BT01040

Morrow, K.H., 2023. A Scale Problem with the Ecosystem Services Argument for Protecting Biodiversity. Environmental Values 32, 271–290. https://doi.org/10.3197/096327122X16569260361751

NSW Department of Primary Industries, 2020. Agricultural production in New South Wales: Crop statistics. NSW Government.

Odgers, N.P., Libohova, Z., Thompson, J.A., 2012. Equal-area spline functions applied to a legacy soil database to create weighted-means maps of soil organic carbon at a continental scale. Geoderma 189–190, 153–163. https://doi.org/10.1016/j.geoderma.2012.05.026

968 Odom, W., Doctor, D., 2023. Rapid estimation of minimum depth-to-bedrock from lidar leveraging deep-
969 learning-derived surficial material maps. Applied Computing and Geosciences 18, 100116.
970 https://doi.org/10.1016/j.acags.2023.100116
971 Pain, C., Gregory, L., Wilson, P., McKenzie, N., 2011. Physiographic Regions of Australia.
972 https://doi.org/10.25919/52XM-CH28
973 Pandey, A.V., Manivannan, A., Nov, O., Satterthwaite, M., Bertini, E., 2014. The Persuasive Power of
974 Data Visualization. IEEE Trans. Visual. Comput. Graphics 20, 2211–2220.
975 https://doi.org/10.1109/TVCG.2014.2346419
976 Pei, J., Li, J., Luo, Y., Rillig, M.C., Smith, P., Gao, W., Li, B., Fang, C., Nie, M., 2025. Patterns and
977 drivers of soil microbial carbon use efficiency across soil depths in forest ecosystems. Nat
978 Commun 16, 5218. https://doi.org/10.1038/s41467-025-60594-8
979 Ponce-Hernandez, R., Marriott, F.H.C., Beckett, P.H.T., 1986. An improved method for reconstructing a
980 soil profile from analyses of a small number of samples. Journal of Soil Science 37, 455–467.
981 Probst, A.J., Ladd, B., Jarett, J.K., Geller-McGrath, D.E., Sieber, C.M.K., Emerson, J.B., Anantharaman,
982 K., Thomas, B.C., Malmstrom, R.R., Stieglmeier, M., Klingl, A., Woyke, T., Ryan, M.C.,
983 Banfield, J.F., 2018. Differential depth distribution of microbial function and putative symbionts
984 through sediment-hosted aquifers in the deep terrestrial subsurface. Nat Microbiol 3, 328–336.
985 https://doi.org/10.1038/s41564-017-0098-y
986 Radočaj, D., Jurišić, M., Rapčan, I., Domazetović, F., Milošević, R., Plaščak, I., 2023. An Independent
987 Validation of SoilGrids Accuracy for Soil Texture Components in Croatia. Land 12, 1034.
988 https://doi.org/10.3390/land12051034
989 Rogozovsky, I., Ansmann, A., Hofer, J., Chudnovsky, A., 2025. Unveiling Atmospheric Layers: Vertical
990 Pollution Patterns and Prospects for High-Resolution Aerosol Retrievals Using the Eastern
991 Mediterranean as a Case Study. Environ. Sci. Technol. 59, 12181–12195.
992 https://doi.org/10.1021/acs.est.4c14556

993 Ruiz, O.E., Wagenaar, J.B., Mehta, B., Ziogas, I., Swanson, L., Worley, K.C., Cruz-Almeida, Y., Johnson,
994 A.J., Boline, J., Boccanfuso, J., Martone, M.E., Haelterman, N.A., 2025. A guide to developing
995 harmonized research workflows in a team science context. Experimental Neurology 392, 115333.
996 https://doi.org/10.1016/j.expneurol.2025.115333
997 Russell, J.S., Moore, A.W., 1968. Comparison of different depth weighting in the numerical analysis of
998 anisotropic soil profile data. Presented at the Transaction of the 9th International Congress,
999 International Soil Science Society, Adelaide, Australia, pp. 205–213.
1000 Sabbaghi, M.A., Esfandiari, M., Eftekhari, K., Torkashvand, A.M., 2024. Predictive map of soil texture
1001 classes using decision tree model and neural network with features of geomorphology level. Can.
1002 J. Soil. Sci. 104, 72–90. https://doi.org/10.1139/cjss-2023-0011
1003 Schaetzl, R.J., Thompson, M.L., 2015. Soils: genesis and geomorphology, Second edition. ed. Cambridge
1004 University Press, New York, NY.
1005 Scott, B.J., Fenton, I.G., Fanning, A.G., Schumann, W.G., Castleman, L.J.C., 2007. Surface soil acidity
1006 and fertility in the eastern Riverina and Western Slopes of southern New South Wales. Aust. J.
1007 Exp. Agric. 47, 949. https://doi.org/10.1071/EA05155x
1008 Searle, R., 2021. Soil and Landscape Grid National Soil Attribute Maps - Australian Soil Classification
1009 Map (3" resolution) - Release 1. https://doi.org/10.25919/VKJN-3013
1010 Simperegui, K.B.D., Kouame, A.K.K., Kwesie, B., Bindraban, P.S., Adzawla, W., Asamoah, E., El
1011 Gharous, M., 2025. Digital mapping of Ghana's soil properties and nutrients: performance of
1012 spline and weighted average approaches. Geoderma 459.
1013 https://doi.org/10.1016/j.geoderma.2025.117365
1014 Smith, J.A., Robert B. Thompson, 2019. Livestock Production in New South Wales: Current Trends and
1015 Future Projections. Australian Journal of Agricultural Science 54, 125–140.
1016 Souza, L.F.T., Hirmas, D.R., Sullivan, P.L., Reuman, D.C., Kirk, M.F., Li, L., Ajami, H., Wen, H., Sarto,
1017 M.V.M., Loecke, T.D., Rudick, A.K., Rice, C.W., Billings, S.A., 2023. Root distributions,

precipitation, and soil structure converge to govern soil organic carbon depth distributions. Geoderma 437, 116569. https://doi.org/10.1016/j.geoderma.2023.116569

Vereecken, H., Schnepf, A., Hopmans, J.W., Javaux, M., Or, D., Roose, T., Vanderborght, J., Young, M.H., Amelung, W., Aitkenhead, M., Allison, S.D., Assouline, S., Baveye, P., Berli, M., Brüggemann, N., Finke, P., Flury, M., Gaiser, T., Govers, G., Ghezzehei, T., Hallett, P., Hendricks Franssen, H.J., Heppell, J., Horn, R., Huisman, J.A., Jacques, D., Jonard, F., Kollet, S., Lafolie, F., Lamorski, K., Leitner, D., McBratney, A., Minasny, B., Montzka, C., Nowak, W., Pachepsky, Y., Padarian, J., Romano, N., Roth, K., Rothfuss, Y., Rowe, E.C., Schwen, A., Šimůnek, J., Tiktak, A., Van Dam, J., Van Der Zee, S.E.A.T.M., Vogel, H.J., Vrugt, J.A., Wöhling, T., Young, I.M., 2016. Modeling Soil Processes: Review, Key Challenges, and New Perspectives. Vadose Zone Journal 15, 1–57. https://doi.org/10.2136/vzj2015.09.0131

Vigués Jorba, J., Scherrer, D., Duchenne, F., Zellweger, F., Gossner, M.M., Bollmann, K., 2025. Differential responses of taxonomic, functional and phylogenetic multi-taxa diversity to environmental factors in temperate forest ecosystems. Ecological Indicators 178, 113855. https://doi.org/10.1016/j.ecolind.2025.113855

Viscarra Rossel, R., Chen, C., Grundy, M., Searle, R., Clifford, D., Odgers, N., Holmes, K., Griffin, T., Liddicoat, C., Kidd, D., 2014. Soil and Landscape Grid National Soil Attribute Maps - Soil Depth (3" resolution) - Release 1. https://doi.org/10.4225/08/546F540FE10AA

Weiskopf, S.R., Myers, B.J.E., Arce-Plata, M.I., Blanchard, J.L., Ferrier, S., Fulton, E.A., Harfoot, M., Isbell, F., Johnson, J.A., Mori, A.S., Weng, E., HarmáCˇková, Z.V., Londoño-Murcia, M.C., Miller, B.W., Pereira, L.M., Rosa, I.M.D., 2022. A Conceptual Framework to Integrate Biodiversity, Ecosystem Function, and Ecosystem Service Models. BioScience 72, 1062–1073. https://doi.org/10.1093/biosci/biac074

Wiese, L., Ros, I., Rozanov, A., Boshoff, A., de Clercq, W., Seifert, T., 2016. An approach to soil carbon accounting and mapping using vertical distribution functions for known soil types. Geoderma 263, 264–273. https://doi.org/10.1016/j.geoderma.2015.07.012

Yanofsky, N.S., 2015. Computability and Complexity of Categorical Structures. https://doi.org/10.48550/ARXIV.1507.05305

Zhang, J., Goodchild, M.F., 2002. Uncertainty in Geographical Information, 0 ed. CRC Press. https://doi.org/10.1201/b12624

Zhang, X., Zhang, W.-C., Wu, W., Liu, H.-B., 2023. Horizontal and vertical variation of soil clay content and its controlling factors in China. Science of The Total Environment 864, 161141. https://doi.org/10.1016/j.scitotenv.2022.161141

Zhao, S., Kvale, K.F., Zhu, L., Zettler, E.R., Egger, M., Mincer, T.J., Amaral-Zettler, L.A., Lebreton, L., Niemann, H., Nakajima, R., Thiel, M., Bos, R.P., Galgani, L., Stubbins, A., 2025. The distribution of subsurface microplastics in the ocean. Nature 641, 51–61. https://doi.org/10.1038/s41586-025-08818-1